Numerical analysis for characterization of reacting and non-reacting spray

Lola Rousseau, Olivier Rouzaud, Mikael Orain, Pascal Fede, Olivier Simonin

Numerical analysis for characterization of reacting and non-reacting spray

Lola ROUSSEAU *[1], Olivier ROUZAUD[1], Mikael ORAIN[2], Pascal FEDE[3], Olivier SIMONIN[3]

[1] ONERA, DMPE, Centre Midi – Pyrénées, 2 Avenue Edouard Belin 31000 Toulouse, France

[2] ONERA, DMPE, Centre Midi – Pyrénées, Rd 53 31410 Mauzac, France

[3] Institut de Mécanique des Fluides de Toulouse (IMFT), Université de Toulouse, CNRS, 2 allées du Professeur Camille Soula 31400 Toulouse, France

*Corresponding author email: lola.rousseau@onera.fr

Abstract

In order to describe droplet spatial distribution in a spray, a numerical study is carried out to firstly, analyse theoretically distributions which could be used to model droplet spatial distribution and secondly, to investigate the influence of acquisition parameters of the optical Mie scattering measurement technique on the experimental characterization of droplet spatial distribution. To this end, the first four moments of the probability density function are compared for the randomly uniformly distribution, the inhomogeneous Poisson distribution and the preferential segregation distribution. Furthermore, a parametric study based on laser sheet thickness and image resolution is performed to determine their influence on droplet spatial distribution. Results show that the first four moments of the inhomogeneous Poisson and the preferential segregation distributions deviate from their theoretical values based on randomly uniformly distribution. Moreover, it is shown that the acquisition and the processing of Mie scattering images acquired from a spray in a three dimensional flow leads to bias on the probability density function and the characterization of the droplet spatial distribution.

Keywords

Spray, Preferential segregation, Inter – droplet distance, Evaporation, Combustion

Funding

The work has been realized thanks to the partial financial support of the "Région Occitanie". The numerical simulations were performed on the supercomputer Olympe (CALMIP) using time available under project P0111 and on the supercomputer Occigen (CINES) under the allocation A0082B0612

Declarations

The authors declare no potential conflicts of interest with respect to the research, authorship, and/or publication of this article

Nomenclature and Units

Latin symbols

G	Group combustion number	[-]
Le	Lewis number	[-]
Sc	Schmidt number	[-]
Re	Reynolds number	[-]
N	Number of droplets	[-]
d	Droplet diameter	[m]
D_i	Mean distance between droplet barycentre	[m]
$\overline{n}$	Droplet density number	[m^{-3}]
r_f	Radius of the flame which surrounds a droplet	[m]
dnn	Nearest-neighbour inter-droplet distance	[m]
$\overline{dnn}$	Mean nearest-neighbour inter-droplet distance	[m]
N_d	Number of droplets in the computational volume	[-]
L	Side length of the cubic computational volume	[m]
e	Slice thickness	[m]
N_s	Number of slices	[-]
St	Stokes number	[-]
St_c	Critical Stokes number	[-]
$E_{transition}$	The relative difference between the nearest-neighbour inter-droplet distance calculated inside the computational volume and the nearest-neighbour inter-droplet distance calculated on the image after the 3D-2D transition	[-]
R	Image resolution	[m^{-1}]

Greek symbols

α	Dimensionless mean of the nearest-neighbour inter-droplet distance distribution	[-]
β	Dimensionless standard deviation of the nearest-neighbour inter-droplet distance distribution	[-]
δ	Dimensionless skewness of the nearest-neighbour inter-droplet distance distribution	[-]
ϵ	Dimensionless kurtosis of the nearest-neighbour inter-droplet distance distribution	[-]
σ_{dnn}	Standard deviation of the mean nearest-neighbour inter-droplet distance	[μm^2]
η	Droplet regular distance	[m]
τ_k	Kolmogorov time scale	[s]
τ_p	Particle relaxation time	[s]
$(\Delta\overline{n})_{adim}$	dimensionless droplet density number gradient	[-]
$\Delta(px)$	Size of a pixel	[m]

Subscripts and superscripts

$2D$	Two dimensions
$3D$	Three dimensions

Acronyms

PLIF	Planar Laser Induced Fluorescence

ILIDS Interferometry Laser Imaging for Droplet Sizing
LACOM Laboratoire de Combustion Multiphasique
PIV Particles Image Velocimetry
HC Hertz-Chandrasekhar
DNS – DPS Direct Numerical Simulation coupled with Discrete Particle Simulation
PDF Probability Density Function

1 Introduction

Gaseous combustion inside a combustion chamber has been studied for decades due to its importance in several industrial applications. In aeroengines, liquid fuel is injected into the combustion chamber as a spray in order to increase heat and mass transfer surfaces between fuel and oxidizer, and thus, improves combustion efficiency. Nevertheless, spray combustion requires a specific attention because it involves a two-phase flow where many phenomena such as atomization, droplet dispersion by turbulence or spray evaporation affect the combustion process and interact with each other. Among all these questions, a point of interest is to determine the influence of the collective effects between droplets on their evaporation and combustion.

In order to better understand the spray combustion, many theoretical, numerical and experimental studies have been conducted about both academic and more realistic configurations. Experimentally, seminal works provided by Godsave (1953) and Spalding (1953) are focused on the ideal case of an isolated droplet burning in a quiescent atmosphere. Nonetheless, isolated droplet is not representative of a spray. To be more realistic, complexity has been gradually added by studying monodispersed droplet streams (Labowsky 1976; Silverman et al. 1994; Orain et al. 2005) and polydispersed spray (Li et al. 1993; Chen et al. 1997; Mikami et al. 2009). In parallel, several models have been developed in order to describe more accurately spray evaporation and combustion in attendance of convective effects (Williams 1973; Abramzon et al. 1989; Jiang et al. 1995; Sirignano 2014). Moreover, some research groups have proposed theoretical models in order to describe better spray evaporation and combustion. We can mention Chiu and co-workers (Suzuki et al. 1971; Chiu et al. 1977, 1982) which have used parameters such as inter-droplet distance and droplet diameter to describe and model the evaporation and the combustion of a monodisperse spray where droplets are distributed according to a simple regular grid. As a result, the "group combustion theory" has been proposed where droplets can burn according to four combustion regimes: single droplet combustion, internal group combustion, external group combustion and external sheath combustion. These regimes are determined from the group combustion number G defined by:

$$G = \frac{1.5Le * \left(1 + 0.276 * Sc^{\frac{1}{3}} * Re^{\frac{1}{2}}\right) * N^{\frac{2}{3}} * d}{D_i} \quad \textbf{(1-1)}$$

where Le, Sc and Re are, respectively, the Lewis, the Schmidt and the Reynolds numbers, N represents the total number of droplets contained in the group, d is the droplet diameter and D_i is equal to the mean distance between droplet barycentre. D_i is deduced from the droplet density number of the group $\overline{n}$. In the 2000's, Réveillon et al. (2005) performed direct numerical simulation of dilute spray and proposed some improvements to this theory. We could also mention Kerstein et al. (1982) which proposed the "percolate combustion model" for a partially premixed flow where three combustion regimes can be distinguished. Each regime is defined according to the following criterion:

$$S = n_v^{\frac{1}{3}} * r_f = \frac{r_f}{\delta_s} \quad \textbf{(1-2)}$$

where n_v is the droplet number density, r_f is the radius of the flame which surrounds a droplet and δ_s is the distance between two droplets. The value of S defines the combustion regime. For $S < 0.41$, the configuration corresponds to a dilute spray where small groups of droplets are surrounded by flames. For $S > 0.73$, the configuration is that of a dense spray where pockets

of gas are surrounded by flames. In the intermediate combustion regime, both previous situations occur. The isolated droplet combustion regime is reached as a particular regime when S tends to zero.

In these theoretical models, it is usually assumed that the droplet spatial distribution is fixed as a simple regular grid distribution, so the droplets are regularly arranged in the spray, and the droplet distance is deduced from the mean density of droplet in the spray (Chiu et al. 1982; Paulhiac 2015). These assumptions have been used in several numerical simulations and experiments. For example, in the numerical study of multi-droplet arrays by Imaoka et al. (2005) and the experimental study by Chauveau et al. (2006), droplets are regularly arranged along the edges of a cube in order to understand the influence of the droplet localisation in the group and the inter-droplet distance on their evaporation and combustion. Results show that the ambient temperature, the number of droplets in the array and their localisation as well as the distance between droplets have an influence on their evaporation and combustion. However, this assumption of a simple regular grid distribution is an oversimplification of the real spatial droplet distribution in a spray. For this reason, it is important to be able to describe more precisely the droplets distribution in a spray. A brief literature survey shows that this issue is also relevant to a variety of research fields. This includes, for example, meteorology, in the context of cloud formation (Kostinski et al. 2001; Shaw et al. 2002) or astrophysics, for stellar dynamics (Chandrasekhar 1943). For the last quoted, a theoretical uniform random distribution law, also called Hertz-Chandrasekhar law (Hertz 1909; Chandrasekhar 1943), has been proposed in order to describe the motion of stars from the average distribution of the other distant stars.

However, these models are only theoretical and, so far, only a few studies are in the open literature attempt to verify their predictions. Numerically, Squires et al. (1991) and Février et al. (2001) have studied the influence of the turbulence on particle distribution in a turbulent flow. Results highlight the emergence of a phenomenon of preferential segregation and show that this effect does not rely on a specific turbulent scale in the flow but rather on the response time of the particle. Experimentally, Sahu et al. (2014, 2016, 2018) have realized one of the most comprehensive study to attempt to describe and understand the interactions between the turbulent flow, the droplet spatial distribution and the droplet evaporation. They have used simultaneously the optical laser techniques of Interferometry Laser Imaging for Droplet Sizing (ILIDS) and Planar Laser Induced Fluorescence (PLIF) to investigate a non-evaporating water spray and an evaporating acetone spray at atmospheric pressure and ambient temperature. This works provides correlations between spray density, vapour mass fraction and droplet velocity and size. Moreover, the authors have found that the vapour spatial concentration was heterogeneous in the flow and connected to the presence of droplet clusters. Finally, it is interesting to note that they have used a parameter G_v, which corresponds to the group evaporating number defined in Chiu's theory.

In order to study spray behaviour under reactive and non-reactive conditions, the experimental test rig PROMETHEE has been developed at the ONERA (Vicentini 2015; Rouzaud et al. 2016). This facility provides flow conditions close to those encountered inside aero-engine combustion chamber. In the studies carried out later on PROMETHEE data (Rousseau et al. 2021; Rouzaud et al. 2021), the authors are especially interested to the nearest-neighbour inter-droplet distance which represents the smallest Euclidian distance between a droplet and its nearest-neighbour in the spray. They show that, for non-reactive and reactive conditions, a linear relationship between the inverse square root of the droplet density number and the mean (resp. standard deviation) nearest-neighbour inter-droplet distance exists, although with different slopes. Moreover, the study of the dimensionless mean of the nearest-neighbour inter-droplet distance distribution α and the associated standard deviation β, demonstrates that the experimental droplet spatial distribution, obtained from Mie scattering

images, is close to the theoretical 2D uniformly randomly distribution at least for droplet density number over 100 droplets per cm². In addition, in order to compare theoretical distribution with experimental results, Rousseau et al. (2021) shows the evolution of the mean nearest-neighbour inter-droplet distance and the standard deviation according to the mean droplet density number by means of a scatter plot, also called mean (resp. standard deviation) dnn – droplet density diagrams. The slope of the scatter plot corresponds to α (resp. β). From these diagrams, the authors have observed two different regions. The first one corresponds to high droplet density numbers and the scatter plot is almost perfectly aligned on the random 2D Hertz-Chandrasekhar distribution. The second one corresponds to low droplet density numbers and there is a slope discontinuity where the scatter plot deviates from the 2D Hertz-Chandrasekhar distribution and its spreading increases. The origin of this discrepancy has not been clearly identified but the authors suggest two possibilities. Firstly, the planar Mie scattering technique provides only two-dimensional images. Therefore, calculating the nearest-neighbour inter-droplet distance, or any distance, from the images implies necessarily some approximations since the transversal dimension is not taken into account. Secondly, Rouzaud et al. (2016, 2021) and Boutsikakis (2020) show that preferential segregation effects have also an influence on α and β and thus can impact the scatter plot of the dnn – density diagram.

This short review shows that the droplet spatial distribution is an essential information for theoretical models and for numerical and experimental studies about evaporation and combustion phenomena in a spray. Having in mind the characterization of the droplet spatial distribution in a spray, this paper focuses on two specific objectives. The first one is to compare theoretically the Hertz-Chandrasekhar distribution, the inhomogeneous Poisson distribution and the preferential segregation distribution, which may be used to describe the droplet spatial distribution in a spray. Their first four moments and their probability density function are studied in order to see how they could be useful to distinguish experimentally these three distributions. The second objective is to study the influence of some experimental acquisition parameters, specific to optical measurement technique, on the characterization of the droplet spatial distribution. The attention is focused on the Mie scattering techniques and its image processing developed by Rousseau et al. (2021). The influence of the laser sheet thickness and the image resolution are studied.

The paper is organised as follow. The first part is dedicated to the presentation of the theoretical laws used to define the distributions studied. Afterwards, the experimental and numerical databases and the data processing employed in this study are described. In the second part, the comparison of the Hertz-Chandrasekhar, inhomogeneous Poisson and preferential segregation distributions is firstly shown. Then comes the study of the influence of the laser sheet thickness on the Hertz-Chandrasekhar distribution and on the preferential segregation distribution. The third part is devoted to the parametric study of the image resolution according to droplet density number in order to see the influence of this parameter on the characterization of the 2D Hertz-Chandrasekhar distribution. Finally, to show an example of application on experimental results, a section is dedicated to a preliminary study of the droplet spatial distribution characterization for the experimental Mie scattering image data for a reactive case. The paper ends with a summary of the main findings and the perspectives.

2 Materials and methods

2.1 Mathematical tools to describe droplet spatial distribution

2.1.1 Characterisation of a distribution

With the aim of characterizing a spray, it is interesting to consider its nearest-neighbour inter-droplet distance (named dnn throughout the paper), possibly at a local scale, and its spatial distribution. The dnn represents the smallest Euclidian distance between a droplet "d" and its nearest-neighbour "d^*" and is expressed in the three-dimensional case as:

$$dnn_{3D}^{d} = \sqrt{(x_d - x_{d^*})^2 + (y_d - y_{d*})^2 + (z_d - z_{d*})^2} \quad \textbf{(2-1)}$$

or, in the two-dimensional case as:

$$dnn_{2D} = \sqrt{(x_d - x_{d^*})^2 + (y_d - y_{d*})^2} \quad \textbf{(2-2)}$$

Hereinafter, we describe the probability density function (pdf) of the nearest-neighbour inter-droplet distance dnn inside a spray. In order to do so, the values of the first four moments will be calculated in the subsequent paragraphs.

According to Lumley (1970), the values of the first four moments give information about the shape of the pdf. While the first moment provides the mean value of the distance $\overline{dnn}$, the second moment σ_{dnn} gives information about the width of the pdf. The third moment corresponds to the "skewness" δ_{dnn} and its value enables to know if the density function is symmetrical or asymmetrical. If δ_{dnn} is equal to zero, the pdf is symmetrical. If δ_{dnn} is positive, the tail which represents larger values than the mean is larger than the tail which represents lower values and conversely when δ_{dnn} is negative. Finally, the fourth moment corresponds to the "kurtosis" ϵ_{dnn} and represents the spreading of the tails toward low and high values. The pdf of the different dnn distribution presented in the paper will be compared to the theoretical law proposed by Hertz-Chandrasekhar (Hertz 1909, Chandrasekhar 1943) thanks to these four first order moments.

2.1.2 Theoretical laws

The regular grid distribution supposes that droplets are regularly arranged inside the spray. This distribution is commonly used in several theoretical or computational studies like those of Chiu et al. (1977) or Paulhiac (2015) but is very far from any true experimental distribution and will not be considered in this paper. Moreover, Rouzaud et al. (2021) and Rousseau et al. (2021) have shown that their experimental results are closer to the Hertz-Chandrasekhar distribution (HC). The HC dnn distribution is derived for a uniform random independent distribution of particles associated to the Poisson distribution of the droplet density number:

$$P(\lambda, k) = \frac{\lambda^k}{k!}\exp(-\lambda) \quad \textbf{(2-3)}$$

where k is the number of droplets enclosed in a volume, ! is the factorial function, λ is the mean droplet number enclosed in the volume which corresponds to the product of the mean droplet density number and the volume and $P(\lambda, k)$ the probability to find k droplets when the mean droplet number is equal to λ.

In the three-dimensional case (3D), the first four moments of the HC distribution can be expressed according to the following relationships:

$$\begin{cases} \overline{dnn_{3D}} = \alpha_{3D} \times \overline{n_{3D}}^{-\frac{1}{3}} \\ \sigma_{dnn_{3D}} = \beta_{3D} \times \overline{n_{3D}}^{-\frac{1}{3}} \\ \delta_{dnn_{3D}} = constant \\ \epsilon_{dnn_{3D}} = constant \end{cases} \quad \textbf{(2-4)}$$

where $\overline{n_{3D}}$ is the mean 3D droplet density number, α_{3D} the corresponding 3D dimensionless mean value of the pdf, β_{3D} the 3D dimensionless standard deviation of the pdf, $\delta_{dnn_{3D}}$ the skewness and $\epsilon_{dnn_{3D}}$ the kurtosis. These last two values do not depend on the volume droplet density number. In order to study distribution of cluster, Milchev (1994) considers stochastic properties and proposes an expression for the dimensionless mean value in three and two dimensions. To complete the definition of these dimensionless parameters, after some algebraic calculations the values of the dimensionless parameters are equal to:

$$\begin{cases} \alpha_{3D} = \Gamma\left(\frac{4}{3}\right) \times \left(\frac{3}{4\pi}\right)^{\frac{1}{3}} \approx 0.5539 \\ \beta_{3D} = \left(\frac{3}{4\pi}\right)^{\frac{1}{3}} \times \left(\Gamma\left(\frac{5}{3}\right) - \Gamma\left(\frac{4}{3}\right)^2\right)^{\frac{1}{2}} \approx 0.2013 \\ \delta_{dnn_{3D}} = \frac{3\Gamma(2)}{4\pi\beta^3} - \frac{3\alpha_{3D}}{\beta_{3D}} - \left(\frac{\alpha_{3D}}{\beta_{3D}}\right)^3 \approx 0.1788 \\ \epsilon_{dnn_{3D}} = \Gamma\left(\frac{7}{3}\right) \times \frac{\left(\frac{3}{4\pi}\right)^{\frac{4}{3}}}{\beta_{3D}^4} - \frac{3\alpha_{3D}\Gamma(2)}{\pi\beta_{3D}^4} + \frac{6\alpha_{3D}^2}{\beta_{3D}^2} + 3\left(\frac{\alpha_{3D}}{\beta_{3D}}\right)^4 \approx 2.6659 \end{cases} \quad \textbf{(2-5)}$$

The same approach stands in the two-dimensional case and the first four moments of the 2D dnn distribution are similarly expressed but using the 2D mean droplet density number $\overline{n_{2D}}$. The values of the dimensionless parameters are approximated as:

$$\begin{cases} \alpha_{2D} \approx 0.50 \\ \beta_{2D} \approx 0.2613 \\ \delta_{dnn_{2D}} \approx 0.6343 \\ \epsilon_{dnn_{2D}} \approx 3.2377 \end{cases} \quad \textbf{(2-6)}$$

2.2 Experimental database

2.2.1 Experimental test rig and operating conditions

In order to study experimentally the spray behaviour under non-reacting and reacting conditions, the experimental test rig PROMETHEE (Figure 1) has been developed and installed on the ONERA LACOM test facility. The flow configuration has been designed to provide flow conditions close to those encountered inside a gas turbine combustion chamber. A full description of this experimental rig has been previously done (Vicentini 2016; Rouzaud et al., 2021) so only a brief description is given here. The LACOM facility enables to supply an air mass flow up to 1 $kg.s^{-1}$ at a maximal temperature of 900 K and a sonic nozzle is used to measure the mass flow rate value. The maximal liquid fuel mass flow rate is equal to 100 $g.s^{-1}$ and the liquid is injected inside the circuit at the ambient temperature. Between its entrance in the circuit and its injection inside the combustion chamber by the injector, the liquid is heated through conduction by the air flow. A Coriolis flow controller provides the actual mass flow rate value during the experiments. The reference combustion chamber has a rectangular shape with an internal square section of 120 x 120 mm^2 and is cooled by a water circuit under reacting conditions. Its four walls are equipped with UV–transparent fused silica windows in order to allow non–intrusive optical measurement. To initiate the combustion, a hydrogen–oxygen torch device is used to ignite the fuel–air mixture. Finally, the burnt gases flow into the exhaust pipe where they are cooled down by means of a water injection shower prior to their ejection in the atmosphere.

Concerning the PROMETHEE test rig, a flow generator located downstream of the sonic nozzle creates a turbulent flow of which the turbulence level is controlled by using several grids. A trapezoidal-shape bluff-body is placed at the entrance of the combustion chamber and is used as a flame holder. It also serves to support the flat-fan spray nozzle for the liquid fuel injection. The nozzle is fixed at the rear of the bluff-body, in the central position. It generates an elliptical-shaped polydisperse spray approximately located around the vertical median plane of the combustion chamber. Due to the presence of the obstacle, vortex shedding occurs under non-reacting conditions with a Strouhal number based on the bulk airflow velocity and the height of the obstacle of 0.28 while the main frequency of the vortex shedding is around 23 Hz. Under reacting conditions, the shedding disappears as expected (Shanbhogue et al. 2009).

Several tests have been conducted under both non–reacting and reacting conditions (Vicentini, 2016). The incoming air flow is heated at 450 K and is at standard atmospheric pressure. The liquid fuel is n-decane at 95 % of purity and is injected in the combustion chamber with an initial temperature of 330 K since the warm air flow heated it. Fuel and air mass flow rates are, respectively, equal to 1 $g.s^{-1}$ and 58 $g.s^{-1}$ and the global ratio is around 0.24. The mean air flow velocity is equal to 5.8 $m.s^{-1}$, such that the Reynolds number based on the height of the bluff – body is about 22 000.

2.2.2 Measurements techniques

Several optical measurement techniques have been used to characterize the two-phase flow inside the combustion chamber under non-reacting and reacting conditions and, subsequently, to build an experimental database. Such a database aims at providing a better understanding of the two-phase flow behaviour and at supporting the validation of the numerical tools. The gaseous phase is characterized by means of the Particles Image Velocimetry (PIV) technique and pressure transducers located on the upper and the lower parts of the bluff-body. PIV allows measuring the velocity field and highlighting some of the

macroscopic structures of the flow like the recirculation zone located behind the obstacle. The pressure transducers are only used to detect the vortex-shedding phenomenon occurring under non–reacting conditions. The liquid phase is characterized by the Mie scattering and Phase Doppler Anemometry (PDA) techniques. The first technique provides the droplets location in the flow, thus allowing to deduce the spatial droplet distribution in the spray. The second one provides local information about droplet diameter and velocity. Under reacting conditions, the OH Planar Laser–Induced Fluorescence (OH-PLIF) and the chemiluminescence emission from OH* (where * indicates that the radical is in an excited electronic state) techniques have also been applied in order to detect the flame front and investigate its interaction with the spray.

In this paper, we will only present the results from Mie scattering images, thus only the Mie scattering installation is described. This technique operates by a Nd:YLF laser (from Quantronix) which has a wavelength of 527 nanometres, a pulse duration about 200 nanoseconds and an energy per pulse equal to 10 milliJoules. The laser beam is transformed into a 1 mm thickness laser sheet that illuminates the two-phase flow. A Phantom V341 high-speed camera located at 90° from the laser sheet propagation collects the Mie scattering signal. The camera is equipped with an 1800 x 1660 pixel² array and its dynamic range is 12 – bit digitization (0 – 4095 counts). In order to have an adequate image resolution to study the flow phenomena, the field of view is chosen smaller than the height of the combustion chamber. The observed field represents 51 x 46 mm² so the spatial resolution is roughly 29 micrometers per pixel. Therefore, to visualize two-phase flow behaviour in the whole combustion chamber, the upper part of the combustion chamber and the lower part are observed.

2.2.3 Mie scattering images collection

For non-reacting conditions, only the upper part of the channel flow has been visualized. The data set is composed of around 3 800 raw Mie scattering images and is linked with the differential pressure signal recorded simultaneously. The pressure signal is periodic due to the presence of a von Karmàn street downstream the bluff-body. The combination of the Mie images and this signal enables to obtain phase-averaged values.

For reacting conditions, upper and lower part of the combustion chamber have been visualized and the data set is still composed of around 3 800 raw Mie scattering images. Conversely, to the non-reactive case, the pressure signal is no longer periodic with the occurrence of the combustion.

2.2.4 Mie scattering image processing algorithm

With the aim of studying the dnn and evaluate the droplet number density, a processing algorithm for the Mie scattering images has been developed by Vicentini (2016) and subsequently improved by Rousseau et al. (2020). The main steps of this algorithm are detailed hereafter.

Firstly, a combination of morphological dilatations with a disk-shaped structuring element and arithmetic operations is applied to the images in order to extract the droplet shapes. Secondly, a binarization operation is performed to the image of the droplet contours to bring droplets out of the image background. Afterwards, a blob analysis is used to identify all the droplets and the locations of their barycentre providing, for each image, the barycentre map. Finally, geometrical and statistical studies on the barycentre maps allow to obtain the map of the 2D droplet density number $\overline{n_{2D}}$ (Figure 2 a), and the map of the mean ($\overline{dnn_{2D}}$) (Figure 2 b) and of the standard deviation ($\sigma_{dnn_{2D}}$) of dnn. From these maps, we obtain two diagrams (Figure 2 c and d) describing the mean dnn (resp. standard deviation) values versus the inverse

of the square root of the 2D droplet density number. The green line corresponds to the 2D dimensionless mean and standard deviation of the simple regular model while the red one corresponds to the dimensionless mean and standard deviation of the 2D HC distribution. From these two figures, the spray distribution is very close to the 2D HC while the simple regular grid model provides a poor estimation of the spray distribution. Consequently, we will only consider the Hertz-Chandrasekhar distribution throughout this paper.

2.3 Numerical data processing

This paragraph describes the main mathematical definitions used to perform the data processing presented hereafter. We describe processes used in the subsequent analysis of the data. The first process concerns the transition from a 3-dimensional droplet field to its 2-dimensional projection on an image acquired by an optical diagnosis (laser sheet + camera in our case). This is schematically described in Figure 3 and it will be called the 3D-2D transition process throughout the paper.

This process is subdivided into two steps: firstly, the transition from a 3D cubic droplet field to a 3D slice (representative of a laser sheet) and secondly, the projection of this slice on a 2D surface (representative of an image acquired by a camera). These two steps are respectively called the slice restriction step and the projection step. In the figure, the lengths L and e correspond respectively to the cube/slice/image side and to the slice thickness. Since each geometry has its own number of droplets, some further notations are introduced to specify the associated droplet density numbers and the nearest-neighbour droplet distance. In the 3D cubic volume with N_d droplets, the mean droplet density number is written as $\overline{n_{3D}} = \frac{N_d}{L^3}$ while the mean nearest-neighbour droplet distance is defined as:

$$\overline{dnn_{3D}} = \frac{1}{N_d}\sum_{d=1}^{N_d} dnn_{3D}^{d} \qquad \textbf{(2-7)}$$

where the distance dnn_{3D}^{d} between a droplet "d" and its nearest-neighbour "d^*" has been previously defined by equation (2-1).

To evaluate the influence of the restriction step on the dnn value, the 3D volume is divided into a number N_s of slices of thickness e with $N_s = \frac{L}{e}$. Similarly to the 3D cubic volume, we can define the dnn value $dnn_{3D}^{d,s}$ between a droplet "d" and its nearest-neighbour "d*" inside the slice s. Its mean value is given by:

$$\overline{dnn_{3D}^{restriction}} = \frac{\sum_{s=1}^{Ns}\left(\sum_{d=1}^{N_d^s} dnn_{3D}^{d,s}\right)}{\sum_{s=1}^{N_s} N_d^s} \qquad \textbf{(2-8)}$$

where N_d^s is the number of droplets contained inside the s-th slice. This mean value is not necessarily equal to $\overline{dnn_{3D}}$ due to the slice restriction process since some droplets inside the slice may have their nearest-neighbour droplet out of the slice leading to an error in the estimation of the dnn. For the same reason, a 3D restriction error is associated to the 3D cubic volume and is called the cubic restriction error.

Next, the droplets contained in any slice s are projected on a 2D image of area S_i. For the sake of convenience, the number of images is noted N_i and is equivalent to N_s. We can define a mean surface density number of droplets $\overline{n_{2D}^{projection}}$ and a mean value for the dnn ($\overline{dnn_{2D}^{projection}}$) associated to the images as:

$$\begin{cases} \overline{n_{2D}^{projection}} = \dfrac{\sum_{i=1}^{N_i} N_d^i}{N_i \times S_i} \\ \overline{dnn_{2D}^{projection}} = \dfrac{\sum_{i=1}^{N_i} \left(\sum_{d=1}^{N_d^i} dnn_{2D}^{d,i} \right)}{\sum_{i=1}^{N_i} N_d^i} \end{cases} \quad \textbf{(2-9)}$$

where the distance $dnn_{2D}^{d,i}$ between a droplet "d" and its nearest-neighbour "d^*" in a 2D image has been previously defined by equation (2-2). It is important to notice that the $\overline{dnn_{2D}^{projection}}$ is generally lower than the $\overline{dnn_{3D}^{restriction}}$. The distance between droplets in the slice are, indeed, most of the time greater than their projected 2D counterparts, which is called throughout the paper the projection effect. The same kind of evaluation has been used for the standard deviation, the skewness and the kurtosis.

In another way, it is interesting to see how we can obtain a 3D cubic droplet field from a 2D image data. Experimental data can be used indeed to verify some assumptions and give some information for numerical simulations. However, experimental images provide two-dimensional results while numerical simulations used generally three-dimensional input/output. To this end, the second process is an extrapolation of the 2D image data to obtain a 3D cubic droplet field. This process is called 2D-3D extrapolation process and corresponds to the opposite of the 3D-2D transition since the first step is the extrapolation of the 2D image to a 3D slice and then an extrapolation of the restricted 3D slice to a 3D cubic volume. At first, a 2D image i is defined by its mean droplet density number equal to $\overline{n_{2D}} = \frac{N_d^i}{L^2}$ and its mean nearest-neighbour droplet distance equal to:

$$\overline{dnn_{2D}} = \frac{1}{N_d^i} \sum_{d=1}^{N_d^i} dnn_{2D}^d \quad \textbf{(2-10)}$$

where dnn_{2D}^d is the distance between a droplet "d" and its nearest-neighbour "d*" in the image i (equation (2-2)).

In order to create the extrapolated 3D restricted slice, the mean droplet density number associated to the slice is defined as:

$$\overline{n_{3D}^{restriction}} = \frac{\overline{n_{2D}}}{e} \quad \textbf{(2-11)}$$

Moreover, we assume that if a 2D droplets field is distributed according to the 2D HC distribution then its extrapolation to a 3D field follows the 3D HC law. In this case, the mean nearest-neighbour inter-droplet distance is calculated by:

$$\overline{dnn_{3D}^{restriction}} = \alpha_{3D}^{HC} * \overline{n_{3D}^{restriction}}^{-\frac{1}{3}} \quad \textbf{(2-12)}$$

Lastly, the extrapolation from the 3D restricted slice to the 3D cubic volume is obtained assuming that the droplet density number is homogeneous along the slice's thickness axis so $\overline{n_{3D}} = \overline{n_{3D}^{restriction}}$ and $\overline{dnn_{3D}} = \overline{dnn_{3D}^{restriction}}$.

Finally, 2D synthetic images are processed as the same way than the experimental 2D images. For further details, please refer to the section 2.2.4.

2.4 Numerical database

2.4.1 Hertz-Chandrasekhar database

A Monte-Carlo simulation tool has been developed in MATLAB© to create cubic computational volumes where droplets are uniformly randomly distributed. According to the case under consideration, the mean droplet density number $\overline{n_{3D}}$, the number of droplet N_d and the side length of the computational volume L vary according to the following relationship:

$$\overline{n_{3D}} = \frac{N_d}{L^3} \quad \textbf{(2-13)}$$

Thereafter, throughout the paper, the droplet regular distance η_{3D} is used to make the 3D length values dimensionless and is defined as:

$$\eta_{3D} = \overline{n_{3D}}^{-\frac{1}{3}} \quad \textbf{(2-14)}$$

To investigate the relevancy of the generated database, its statistical convergence has been addressed. To carry out this study, four droplet density number values have been selected from 100 to 3 000 droplets per cm^{-3}, nine dimensionless size of the computational cube $\left(\frac{L}{\eta_{3D}}\right)$ values from approximately 30 up to 90 and the number of droplets N_d varies between 30 000 and 800 000. These droplet density numbers are representative of the aforementioned experimental flow (section 2.2.4). Note that in order to save up some computational time, only one draw has been achieved for each configuration. Assessment of the convergence is based on the calculation of the relative error of the variable X_i defined as:

$$\text{relative error } (X_i) = \frac{X_i - X_i^{HC}}{X_i^{HC}} \quad \textbf{(2-15)}$$

where X_i represents any of the statistical parameters $\alpha_{3D}, \beta_{3D}, \delta_{3D}, \varepsilon_{3D}$ estimated from the numerical database and X_i^{HC} corresponds to the theoretical HC value. The results are presented in Figure 4, the relative errors being plotted versus the dimensionless size of the computational volume.

At first, let us consider a fixed droplet density number. Increasing the dimensionless size is thus equivalent to have a larger statistical sample. As expected, the relative errors of the α_{3D} and β_{3D} parameters decrease with L/η_{3D} in such a case. However, the evolutions of the last

two parameters are less monotonous, in particular for the kurtosis. This observation can be explained by the fact that only one draw is carried out by configuration. Consequently, the value of the dimensionless parameter, and thus of the relative error, can varies around a mean value. This behaviour is more obvious when the moment of the pdf is large (see appendix). One can also consider that the convergence of the parameters α_{3D}, β_{3D} is reached even for the smaller values of the dimensionless size since the relative error is lower than 5% in any case. For the kurtosis ε_{3D}, the agreement with the HC value is weaker but is around 5% for the highest values of the dimensionless size (L/η_{3D} greater than 55). The convergence of the skewness parameter δ_{3D} is poorer, the relative error starting around 45% in the worst case and slowly decreasing around 10 % for L/η_{3D} greater than approximately 65. Despite these deviations for δ_{3D} and β_{3D}, the results demonstrate that the numerical generation reproduces quite fairly a uniformly random distribution. Numerical data provided by the Monte-Carlo simulation tool will be used in the next part (section 3).

Secondly, for the whole droplet density numbers and over a certain value of L/η_{3D}, the points are superimposed which means that the estimation of the relative error for dimensionless parameters is universal. It is interesting since they provide a means to evaluate the quality of the sample. More precisely, given a mean value of the droplet density number, one can derive very simply the minimal size of the volume to reach a certain convergence level based on the previous figures. This value can be compared to the size L provided by a numerical (size of a 3D sampling volume) or an experimental data (size of an image) to estimate the quality of the under study configuration.

Figure 5 shows the comparison of the pdf for the dimensionless distance dnn/η_{3D} between the theoretical 3D HC distribution and the results of the Monte-Carlo simulation for the case of 3D droplet density number equals to 1 000 droplets per cm^3 and the dimensionless size of the computational cube equals to 56. Red solid line corresponds to the pdf of the 3D Hertz-Chandrasekhar distribution function calculated with the mean droplet density number value $\overline{n_{3D}}$ of the Monte-Carlo data and blue histogram corresponds to the pdf obtained with the Monte-Carlo simulation. This figure is consistent with the previous results since it shows that the pdf of the simulation is really close to the theoretical pdf so the numerical generation reproduces quite farily a uniformly random distribution.

2.4.2 Preferential segregation numerical database

To study the effects of the preferential segregation, six Direct Numerical Simulation coupled with Discrete Particle Simulation (DNS – DPS) (Fede et al., 2015) have been used. The computational volume is a cube that contains 140 367 spherical particles with a constant diameter and with a volume droplet density number around 6 x 10^{-4} droplet per cm^{-3}. Consequently, the dimensionless cube size is around 53 and, according to the conclusions of the previous section and assuming that the tendencies drawn for the HC distribution apply to a preferential segregation case, such a value is sufficient to ensure α_{3D}, β_{3D} and ϵ_{3D} are statistically converged. The numerical issue leads to a deviation around 0.5 % on α_{3D}, 1.5 % on β_{3D}, 18 % on δ_{3D} and 5.5 % on ϵ_{3D}. The gaseous flow used is the same for all the simulations and its characteristics are the following. The fluid density is equal to 1 $kg.m^{-3}$, the dynamical viscosity is equal to 10^{-3} $kg.m^{-1}.s^{-1}$, the Kolmogorov distance scale (η_K) is around 17.55 millimetres, the Kolmogorov time scale (τ_K) is around 0.3088 seconds and the Kolmogorov velocity scale is around 0.5691 $m.s^{-1}$. To highlight the preferential segregation effect, the particle mass density varies from 12.5 $kg.cm^{-3}$ to 1 250 $kg.cm^{-3}$. The Stokes particle number is between 0.33 to 14.42 and is defined as follows:

$$St = \frac{\tau_p}{\tau_k} \quad \textbf{(2-16)}$$

where τ_p is the particle relaxation time. Figure 6 shows slices of the droplet spatial distribution in the computational volume according to four different Stokes numbers. For Stokes numbers equal to 1.37 (b) and 5.06 (c), preferential segregation is clearly observed.

2.4.3 Inhomogeneous Poisson database

To reproduce droplet fields with droplet density gradient as observed in the combustion chamber (Figure 2 a), an inhomogeneous Poisson simulation tool has been developed in MATLAB©. This way, 3D and 2D fields are created where droplets are distributed according to an inhomogeneous Poisson law (Shaw et al., 2002). In this case, the probability that a droplet is located between two positions x_1 and x_2 for a given droplet density number is defined by:

$$P(N, x_1, x_2) = \frac{\left(\int_{x_1}^{x_2} \lambda(x)dx\right)^N}{N!} \exp\left(-\int_{x_1}^{x_2} \lambda(x)dx\right) \quad \textbf{(2-17)}$$

where $x \in [x_1; x_2]$, $\overline{N} = \int_{x_1}^{x_2} \lambda(x)dx$ is the mean droplet density number in this interval and λ is a variable process rate.

3 Results

3.1 Comparison specific droplet spatial distributions with respect to the Hertz-Chandrasekhar distribution

In this section, in order to characterize droplet spatial distribution in 3D and 2D, we compare two specific droplet distributions with respect to the HC distribution. Firstly, we study the 3D distribution that takes into account the preferential segregation effects. Secondly, we study in 2D and 3D the inhomogeneous Poisson distribution that takes into account the droplet density gradient.

3.1.1 Preferential segregation distribution

Figure 7 shows the evolution of the dimensionless parameters α_{3D}, β_{3D}, δ_{3D} and ϵ_{3D} according to the Stokes number. The dashed black line corresponds to the results of DNS-DPS simulations (dimensionless cube size equals 53) and these curves are compared to the theoretical values given by the Hertz–Chandrasekhar distribution (HC law, red line). Different observations can be done. Firstly, the evolution of α_{3D} is opposite to those of β_{3D}, δ_{3D} and ϵ_{3D}. Secondly, for all of the parameters, the largest discrepancy according to the theoretical value is reached for the same Stokes number called "critical Stokes" (St_c) and equal to 1.37. Thirdly, for the smallest Stokes number, parameter values tend to their theoretical values. When the Stokes number increases, α_{3D} decreases while β_{3D}, δ_{3D} and ϵ_{3D} increase and they all deviate from their theoretical values. For Stokes numbers higher than St_c, when the Stokes number increases, α_{3D} increases while β_{3D}, δ_{3D} and ϵ_{3D} decrease and they all tend towards the theoretical values for the higher Stokes numbers. This result is consistent with the literature

(Vicentini 2015; Boutsikakis 2020). This can be explained as follows. When the Stokes number is very small, droplets behave as fluid elements and are dispersed everywhere, which is similar to the 3D HC distribution. If the Stokes number increases, the inertia of the particle raises and preferential segregation appears and leads to a clear variation of α_{3D}, β_{3D}, δ_{3D} and ϵ_{3D} parameters when $St = St_c$. Finally, with increasing Stokes number, particles become very inertial and do not track the gaseous flow anymore, leading to a droplet spatial distribution close again to the 3D HC distribution. Therefore, deviations of the dimensionless parameters α_{3D}, β_{3D}, δ_{3D} and ϵ_{3D} are clearly highlighted and can serve as a marker of the presence of preferential segregation.

The study of the dnn Probability Density Function (PDF) is a complementary way to observe preferential segregation. Figure 8**Error! Reference source not found.** shows the PDFs for the dimensionless distance $\frac{dnn_{3D}}{\eta_{3D}}$ for four different Stokes numbers. Red solid line corresponds to the PDF of the 3D Hertz-Chandrasekhar distribution function calculated with the mean droplet density value $\overline{n_{3D}}$ of the DNS-DPS data and blue histogram corresponds to the PDF obtained with the simulations. In any case, the distributions associated to the preferential segregation are shifted towards the left with respect to the theoretical PDF, so the values of the $\overline{dnn_{3D}}$ distance are lower than that for theoretical distribution. The shift value varies with the Stokes number, firstly increasing and then decreasing with a maximal shift obtained for the critical Stokes number St_c. The overall behaviour of the preferential segregation PDFs corroborates the evolution of the dimensionless mean parameter. According to the linear relationship between α_{3D}, $\overline{n_{3D}}$ and $\overline{dnn_{3D}}$ (equation (2-4)), decreasing α_{3D} is equivalent to decreasing $\overline{dnn_{3D}}$ and inversely for a fixed droplet density number. Furthermore, when the PDF is shifted at the left then the asymmetry of the PDF increases and, by definition, δ_{3D} increases.

3.1.2 Inhomogeneous Poisson distribution

In Figure 2 a, the local mean droplet density number $\overline{n_{2D}}$ value decreases along the injector axis and the height of the combustion chamber. Therefore, there is a droplet density gradient inside the combustion chamber. In order to estimate its influence on the dimensionless parameters, 3D and 2D numerical test cases have been built with the inhomogeneous Poisson tool (see section 2.4.3).

3D study:

Three computational parallelepiped volumes have been created with dimensions respectively of 30 x 30 x 30 mm^3, 40 x 30 x 30 mm^3 and 50 x 30 x 30 mm^3 following the axis $[\vec{x}\ \vec{y}\ \vec{z}]$. The dimensions have been chosen in order to have a number of droplets sufficient to perform the analysis but limited to save up some computational time. The droplet density gradient applies along the $\vec{x}$ axis. For this study, we choose the following input parameters. The step between x_1 and x_2 is constant and equal to one millimetre. The maximum droplet density number is located at the volume inlet $x = 0$ and, for each computational volume, is equal to 7 000 droplets per cm^3 and 8 000 droplets per cm^3. The minimum droplet density number is located at the volume outlet x=L (L = 30 mm, 40 mm or 50 mm according to the computational volume) and varies between 500 droplets per cm^3 and 6 000 droplets per cm^3 with a step of 500 droplets per cm^3. The variation of the droplet density number between step is calculated as:

$$\overline{n_{3D}}(x) = \int_{x_1}^{x_2} \left(\overline{n_{3D_{max}}} - \frac{\left(\overline{n_{3D_{max}}} - \overline{n_{3D_{min}}}\right)}{L} x_1 \right) dx \qquad \textbf{(3-1)}$$

For the most restrictive case, which means a minimal droplet density number of 500 droplets per cm^3, a maximal droplet density number of 7 000 droplets per cm^3 and L = 30 mm, the volume contains 98 325 droplets. According to the Figure 4, the error committed on dimensionless parameter values compared to the theoretical value is around 0.7 %, 2 %, 17 % and 6 % for respectively α_{3D}, β_{3D}, δ_{3D} and ϵ_{3D}. Figure 9 shows an example of this inhomogeneous Poisson distribution of droplets.

Hereinafter, we define a configuration as a set of one value for each parameter L and $\overline{n_{max}}$ and where $\overline{n_{min}}$ varies between 500 and 6 000 droplets per cm^3. Table 1 summarizes all the configurations to study the influence of the 3D droplet density gradient on dimensionless parameters α_{3D}, β_{3D}, δ_{3D} and ϵ_{3D}.

We use the relationships (2-1), (2-4) and (2-7) to calculate the global $\overline{dnn_{3D}}$ and $\overline{n_{3D}}$ on the volume and estimate α_{3D}, β_{3D}, δ_{3D} and ϵ_{3D} values depending on the global value of the dimensionless droplet density number gradient. The dimensionless droplet density number gradient is defined according to the relationship:

$$(\Delta\overline{n_{3D}})_{adim} = \frac{\Delta\overline{n_{3D}}}{\overline{n_{3D}}} \qquad \textbf{(3-2)}$$

where $\Delta\overline{n_{3D}}$ corresponds to the droplet density number difference $|\overline{n_{3D}}(x = L) - \overline{n_{3D}}(x = 0)|$ and $\overline{n_{3D}}$ is the total droplet density number in the volume. According to the configuration, the minimal and maximal dimensionless gradient values are respectively equal to 0.1 and 1.80.

Figure 10 shows the evolution of the dimensionless parameters α_{3D}, β_{3D}, δ_{3D} and ϵ_{3D} according to the dimensionless gradient for the six numerical configurations. For each set-up, the dimensionless parameters deviate from the theoretical values for a homogeneous Poisson distribution. When the dimensionless gradient value increases, α_{3D} decreases while β_{3D}, δ_{3D} and ϵ_{3D} increase. A similar evolution is observed when, for Stokes number lower than St_c, the Stokes number increases and the preferential segregation effects are developed in the spray. Nevertheless, the study of the dimensionless parameters according to the Stokes number is linked to the droplet dynamic while the study of the dimensionless parameters according to the dimensionless droplet density gradient is linked directly to the spatial distribution. For this reason, a relationship between preferential segregation and droplet density gradient cannot be drawn. However, it is possible to say that their influence on dimensionless parameters α_{3D}, β_{3D}, δ_{3D} and ϵ_{3D} are similar and we can find some droplet density gradient in the spray when preferential segregation effect is present. Finally, the points are superimposed which means that the estimation of the deviation of dimensionless parameter due to the dimensionless gradient is universal.

While the inhomogeneous case described here is purely theoretical, the existence of droplet density gradient inside a flow is obvious. Such a fact associated to these results means that the deviation of the first four moments can be attributed either to preferential segregation or to an inhomogeneous distribution of the droplets. One can also note that, for the range of gradients selected, the relative error on the α_{3D} parameter is at most equal to 4% while the relative errors for the other parameters are relatively small up to $(\Delta\overline{n_{3D}})_{adim} = 0.7$ and becomes much more significant above this threshold.

2D study:

In the same way as for the 3D study, numerical test case has been built in order to estimate the influence of the 2D droplet density gradient on the dimensionless parameters α_{2D}, β_{2D}, δ_{2D} and ϵ_{2D}. The computational surface is a rectangle with dimensions respectively of 40 x 40 mm², 50 x 40 mm² and 60 x 40 mm² following the axis $[\vec{x}\ \vec{y}]$. The droplet density gradient is along the $\vec{x}$ axis and droplets are distributed according to the inhomogeneous Poisson law defined by the equation (equation (2-17)). The step between x_1 and x_2 is constant and equal to one millimetre. The maximum droplet density number is located at the volume inlet $x = 0$ and, for each computational volume, is equal to 4 000 droplets per cm^2 and 4 500 droplets per cm^2. The variation of the droplet density number between step is calculated as:

$$\overline{n_{2D}}(x) = \int_{x_1}^{x_2} \left(\overline{n_{2D_{max}}} - \frac{\left(\overline{n_{2D_{max}}} - \overline{n_{2D_{min}}}\right)}{L} x_1 \right) dx \qquad \textbf{(3-3)}$$

The minimum droplet density number is located at the surface outlet x=L (L = 40 mm, 50 mm or 60 mm according to the surface) and varies between 10 droplets per cm^2 and 3500 droplets per cm^2. Table 2 summarizes all the configurations to study the influence of the 2D droplet density gradient on dimensionless parameters α_{2D}, β_{2D}, δ_{2D} and ϵ_{2D}. For the most restrictive case, which means a minimal droplet density number of 10 droplets per cm², a maximal droplet density number of 4 000 droplets per cm² and L = 40 mm, the surface contains 31 264 droplets. In this way, L/η_{2D} is equal around 180 and a statistical study allows us to confirm that the statistical convergence is assumed.

The processing algorithm to calculate dimensionless parameters is the same than is previously used for 3D case and depending on the global value of the dimensionless surface droplet density number gradient defined as:

$$(\Delta\overline{n_{2D}})_{adim} = \frac{\Delta\overline{n_{2D}}}{\overline{\overline{n_{2D}}}} \qquad \textbf{(3-4)}$$

where $\Delta\overline{n_{2D}}$ corresponds to the surface droplet density difference $|\overline{n_{2D}}(x = L) - \overline{n_{2D}}(x = 0)|$ and $\overline{\overline{n_{2D}}}$ is the total number of droplets divided by the suface. According to the configuration, the minimal and maximal dimensionless gradient values are respectively equal to 0.1 and 2.2.

Figure 11 shows the evolution of the dimensionless parameters α_{2D}, β_{2D}, δ_{2D} and ϵ_{2D} values according to the dimensionless gradient for the numerical configurations. Similarly to the 3D case, when the dimensionless 2D density gradient increases the dimensionless parameters deviate from the theoretical values for homogeneous Poisson distribution: α_{2D} decreases while β_{2D}, δ_{2D} and ϵ_{2D} increases according to the theoretical value. Just as for 3D case, preferential segregation and inhomogeneous density have a similar influence on the dimensionless parameters α_{2D}, β_{2D}, δ_{2D} and ϵ_{2D}. Nevertheless, a direct correlation between these two effects cannot be established.

3.2 Study of the 3D – 2D transition

3.2.1 Hertz-Chandrasekhar case

Experimental images provide information about a two-dimensional droplet spatial distribution from the three-dimensional droplet field inside the combustion chamber. In order to better understand the experimental results, it is necessary to see the influence of this transition from the 3D to the 2D on the dimensionless parameters α_{2D}, β_{2D}, δ_{2D} and ϵ_{3D} and on the dnn – droplet density number diagram. To this end, a numerical test case has been built from the Monte-Carlo simulation tool described in the section 2.4.1 and the numerical data processing described in section 2.3 is applied. The computational volume is a cube where 200 000 droplets are distributed according to the 3D HC distribution. In order to find the same order of magnitude for the surface droplet density number $\overline{n_{2D}}$ after the 3D-2D transition than in our experiment (Rousseau et al. 2021), $\overline{n_{3D}}$ is defined from the $\overline{n_{2D}}$. Since $\overline{n_{2D}}$ varies between 100 and 5 000 droplets per cm² and the slice thickness e varies between one and three millimetres with a step of one millimetre then the volume droplet density number $\overline{n_{3D}}$ varies between 300 droplets per cm^3 and 50 000 droplet per cm^3. For the most restrictive case, L/η_{3D} is around 60 which means that, according to Figure 4, the error committed on dimensionless parameter values compared to the theoretical value is around 0.5 %, 2 %, 18 % and 5 % for respectively α_{3D}, β_{3D}, δ_{3D} and ϵ_{3D}.

Firstly, the creation of the slice leads to an anisotropic volume where the thickness is much smaller than the two other sides equal to L. A restriction effect appears which can modify the dimensionless parameters α_{3D}, β_{3D}, δ_{3D} and ϵ_{3D}. To this reason, it is interesting to study the influence of the slice thickness on the relative error of the dimensionless parameters (see equation (2-15)). In the same way as for the cubic computational volume, the slice thickness is dimensionless by η_{3D} calculated according to the initial $\overline{n_{3D}}$. Figure 12 shows the evolution of the relative error of $\alpha_{3D}^{restriction}$, $\beta_{3D}^{restriction}$, $\delta_{3D}^{restriction}$ and $\epsilon_{3D}^{restriction}$ according to the dimensionless thickness e/η_{3D} and for three values of the slice thickness e. Several observations can be drawn. Firstly, the relative error calculated for the four dimensionless parameters is considerabely higher than the relative error due to the Monte-Carlo simulations which means that this error can be associated to the restriction effect. Secondly, for $\alpha_{3D}^{restriction}$, the relative error is positive and when the dimensionless thickness increases the relative error decreases to tends towards zeros. If the relative error is positive then $\alpha_{3D}^{restriction}$ is higher than the theoretical value for the 3D HC distribution and the mean dnn in the slice is higher than the theoretical value. This behaviour is expected since some droplets are not taking into account to calculate the dnn which leads to an increase of the dnn value.

The projection step (define in section 2.3) can leads to modification of the droplet spatial distribution. The influence of the slice thickness on the relative error of the dimensionless parameters is studied. Figure 13 shows the evolution of the relative error of $\alpha_{2D}^{projection}$, $\beta_{2D}^{projection}$, $\delta_{2D}^{projection}$ and $\epsilon_{3D}^{projection}$ according to the dimensionless thickness e/η_{2D} and for three values of e. For each dimensionless parameters, the relative error is included in the interval of the relative error due to the Monte-Carlo simulations. It means that $\alpha_{2D}^{projection}$, $\beta_{2D}^{projection}$, $\delta_{2D}^{projection}$ and $\epsilon_{3D}^{projection}$ values are close to the theoretical value for the 2D HC distribution. From this observation, it can be said that the projection of a 3D droplet field obeying the 3D HC distribution leads to a 2D droplet field obeying the 2D HC distribution, thus:

$$\begin{cases} \alpha_{2D}^{projection} = \alpha_{2D}^{HC} \\ \beta_{2D}^{projection} = \beta_{2D}^{HC} \end{cases} \quad \textbf{(3-5)}$$

In the opposite way, it is also interesting to determine the relationship that links a 2D droplet field to a 3D one especially useful for numerical simulations. It is interesting to define a 3D dnn distribution from the 2D dnn distribution calculated according to 2D images (and particularly experimental Mie scattering image). For this reason, it is necessary to evaluate the difference committed on $\overline{dnn_{3D}}$ and $\overline{dnn_{2D}}$ due to the 3D-2D transition.

If the droplet density number is homogeneous in the laser sheet then the relationship between the 3D droplet density number due to the restriction effect and this due to the projection is defined as:

$$\overline{n_{3D}} = \frac{\overline{n_{2D}^{projection}}}{e} \quad \textbf{(3-6)}$$

From the equation (3-6), the relationship between 2D droplet density number obtained after projection and the 2D mean dnn (resp. the 2D standard deviation dnn) is defined as follow:

$$\begin{cases} \overline{dnn_{2D}^{projection}} = \alpha_{2D}^{HC} * \overline{n_{2D}^{projection}}^{-\frac{1}{2}} \\ \sigma_{dnn_{2D}}^{projection} = \beta_{2D}^{HC} * \overline{n_{2D}^{projection}}^{-\frac{1}{2}} \end{cases} \quad \textbf{(3-7)}$$

The relative difference between $\overline{dnn_{3D}}$ calculated inside the volume and the 2D mean dnn calculated on the image after the 3D-2D transition is thus defined as:

$$E_{transition}(\overline{n}, e) = \frac{\overline{dnn_{2D}^{projection}} - \overline{dnn_{3D}}}{\overline{dnn_{3D}}} \quad \textbf{(3-8)}$$

This relative difference can be calculated theoretically as:

$$E_{transition}(\overline{n_{3D}}, e) = \frac{\alpha_{2D}^{HC}}{\alpha_{3D}^{HC}} * e^{-\frac{1}{2}} * \overline{n_{3D}}^{-\frac{1}{6}} - 1$$

or, equivalently

$$E_{transition}\left(\overline{n_{2D}^{projection}}, e\right) = \frac{\alpha_{2D}^{HC}}{\alpha_{3D}^{HC}} * e^{-\frac{1}{3}} * \overline{n_{2D}^{projection}}^{-\frac{1}{6}} - 1 \quad \textbf{(3-9)}$$

The previous numerical test case created to estimate the influence of the relative error on the dimensionless parameters α_{2D}, β_{2D}, δ_{2D} and ϵ_{2D} (Figure 12 and Figure 13) is used again to confirm the equation (3-9). From the characteristics of the projected 2D field, an extrapolation transition from the 2D images to the 3D volume is carried out. It is important to notice that since the 2D field is provided by a projection, there may be some difference according to the theoretical 2D Hertz-Chandrasekhar distribution. Indeed, some droplets in the 3D field can be superimposed or grouped together due to the projection in the 2D field. **Error! Reference source not found.**Figure 14 shows the evolution of $E_{transition}$ according to the

dimensionless thickness. The red line represents the theoretical law defined by the equation (3-9) for the case where $\overline{n_{3D}}$ is fixed and the thickness slice varies continuously. The blue circles, the black squares and the green stars represent the results for the Monte-Carlo simulation in the case of thickness slice e equal respectively to 1, 2 and 3 millimetres. First of all, the results of the test case are really close to the theoretical law which means that a 3D field where droplets are distributed according to the 3D HC distribution is obtained from a 2D droplet field where droplets are distributed according to the 2D HC distribution. Consequently, the 2D-3D extrapolation process defined in section 2.3 is validated. Secondly, it is interesting to notice that the evolution of the relative difference according to the dimensionless thickness $\frac{e}{\eta_{3D}}$ is universal. In summary, for the Hertz-Chandrasekhar case, if the slice thickness e and the $\overline{n_{2D}}$ are known then $E_{transition}$ can be determine with the equation (3-9). Consequently, $\overline{dnn_{3D}}$ can be deduce and allow to calculate $\overline{n_{3D}}$ from the Hertz-Chandrasekhar relationship (equation (2-4)).

3.2.2 Preferential segregation case

It is necessary to extend the study of the 3D-2D transition to a more general case that includes the influence of the preferential segregation effect on the droplet spatial distribution. For this reason, it is interesting to evaluate the difference between the $\overline{dnn_{3D}}$ and the $\overline{dnn_{2D}}$ due to the 3D-2D transition for a droplet field when preferential segregation effects exist.

It is fair to assume that the relationship between the droplet density number, the slice thickness and $E_{transition}$ has the same shape than the one given for the Hertz-Chandrasekhar case (equation (3-9)). However, α_{3D} value depends at least on the Stokes number (section 3.1.1). Moreover, previous work (Rousseau et al., 2021) shows that, for the preferential segregation case, $\alpha_{2D}^{projection}$ and $\beta_{2D}^{projection}$ have a similar behaviour than α_{3D} and β_{3D} according to the Stokes number but their values vary according to the slice thickness e. Therefore, we assume that the relationship for the relative difference between $\overline{dnn_{3D}}$ and $\overline{dnn_{2D}^{projection}}$ is defined as:

$$\begin{cases} E_{transition}\left(\overline{n_{3D}}, e, St, \dfrac{e}{\eta_{3D}}\right) = \dfrac{\alpha_{2D}}{\alpha_{3D}}\left(St, \dfrac{e}{\eta_{3D}}\right) * e^{-\frac{1}{2}} * \overline{n_{3D}}^{-\frac{1}{6}} - 1 \\ E_{transition}\left(\overline{n_{2D}^{projection}}, e, St, \dfrac{e}{\eta_{2D}}\right) = \dfrac{\alpha_{2D}}{\alpha_{3D}}\left(St, \dfrac{e}{\eta_{2D}}\right) * e^{-\frac{1}{3}} * \overline{n_{2D}^{projection}}^{-\frac{1}{6}} - 1 \end{cases} \quad \textbf{(3-10)}$$

In order to estimate $E_{transition}$, it is necessary to evaluate the evolution of α_{2D}/α_{3D} according to the Stokes number and the slice thickness. To this aim, we have reproduced numerically the 3D-2D transition starting from the DNS-DPS simulations in order to create 2D images for with several slices thickness e and estimate an evolution of the ratio α_{2D}/α_{3D} according to the Stokes number and the slice thickness.

Figure 15 shows the evolution of α_{2D}/α_{3D} according to the dimensionless thickness for the six different Stokes numbers of the DNS/DPS simulations. Several remarks can be done. Firstly, the behaviour of the ratio according to the dimensionless thickness is similar for each Stokes number. Starting from a dimensionless thickness value null, the ratio decreases until to reach a minimum value. Afterwards, the ratio increases and tends towards an asymptotic value. Secondly, for each Stokes number, the minimal value of the ratio is obtained for a dimensionless thickness close to 0.75. Thirdly, the minimum value of the ratio and the asymptotic value

depend on the Stokes number. Starting from a null Stokes number, when the Stokes number increases up to its critical value 1.37, the minimum value of α_{2D}/α_{3D} decreases and the asymptotic value increases. Above the critical value, when the Stokes number increases, the minimum value of the ratio increases and the asymptotic value decreases and both values tend towards $\frac{\alpha_{2D}^{HC}}{\alpha_{3D}^{HC}}$. It could be interesting to model the evolution of this ratio in further works.

3.3 Influence of the experimental image acquirement

The ability of an image to reproduce the observed field depends on its resolution R which represents the number of pixel per millimetre. In order to have a better study of the droplet spatial distribution, it is interesting that the image resolution is selected to match with droplet size implying that droplets are mostly represented by several pixels and are more easily detected. In the following, the size in millimetres of a pixel $\Delta(px)$ is defined by:

$$\Delta(px) = \frac{1}{R} \quad \textbf{(3-11)}$$

The resolution can be modified in two ways. Firstly, the camera used is equipped with a fixed pixel array, which is an intrinsic characteristic of the equipment. Therefore, for a same size of observed field, if the camera is changed for another with a larger pixel array, the resolution becomes higher and the pixel size smaller. The second one is by considering a smaller or larger observed field. The largest the field is, the lower the resolution is and inversely. Besides, the droplet detection on the images is linked to image resolution since a droplet with a diameter smaller than the pixel size is represented by one pixel while a droplet with a diameter larger than the pixel size is represented by at least two pixels. Likewise, two droplets have to be separated by at least one pixel in order to be observed separately, otherwise the processing algorithm detects only one droplet.

In order to quantify the influence of the image resolution on the dimensionless parameters $\alpha_{2D}, \beta_{2D}, \delta_{2D}$ and ϵ_{2D} and the PDF of the dnn, synthetic images have been produced considering different image resolutions. The geometry corresponds to a square surface with a length size of 80 millimetres. Firstly, droplets have been distributed according to the 2D Monte-Carlo distribution with six surface droplet density numbers varying between 100 and 4 000 droplets per cm² which represents a ratio L/η_{2D} varying between around 80 and 660. Note that these droplets are only points since they have no diameter. The density numbers are representative values extracted from our experimental data (Rousseau et al., 2021). Starting from these data, a mesh representing the pixel array is built with a uniform step in order to determine the spatial locations of the droplets and to define the coordinates of their barycentre, thus a mesh cell is equivalent to a pixel in a real image. Four different values of the mesh step are used to reproduce the variation of the resolution: 10 pixels per millimetre (pixel length size 0.1 millimetre), 20 pixels per millimetre (pixel length size 0.05 millimetre), 40 pixels per millimetre (pixel length size 0.025 millimetre) and 60 pixels per millimetre (pixel length size 0.0167 millimetre). For each configuration of image resolution and surface droplet density number, 30 synthetic images have been created. If one numerical droplet is located inside the pixel, the level of the pixel is equal to one while it is zero when the pixel is not occupied. If the cell is occupied by more than one numerical droplet, one considers that there is only one droplet attached to this cell and its pixel level is one. Such a process is called droplet aggregation. Table 3 summarises the percentage of droplets loss throughout the transition between the 2D field and the 2D synthetic image due to the droplet aggregation according to the initial configuration.

This phenomenon involves a droplet loss in the numerical image between 0.03 % and 17.61 %. For a droplet density number, if the image resolution increases then the pixel size decreases and the percentage of droplet loss decreases. For example, for a reference initial $\overline{n_{2D}}$ of 4 000 droplets per cm², $\overline{n_{2D}}$ after the creation of the synthetic image is around 3 296 droplets per cm² for $\Delta(px)$ equal to 0.1 mm and around 3 950 droplets per cm² for $\Delta(px)$ equal to 0.0167 mm. Inversely, for a fixed pixel size, if the droplet density number increases, the droplet loss increases.

In a second step, we apply the image processing developed for the study of the experimental Mie scattering image (see part. 2.2.4). The blob analysis is performed on the synthetic image to detect all the droplets and their locations on the mesh. During this stage, some droplets are also merged together because their barycentre are located in neighbouring cells. Table 4 summarises the percentage of lost droplets due to the merging involved during the image process. This percentage is calculated with the number of droplets existing after the creation of the synthetic image. Similarly to the aggregation phenomenon, the droplet loss increases when the droplet density number increases or the image resolution decreases. To illustrate this point, for a pixel size of 0.1 mm, the droplet density number $\overline{n_{2D}}$ calculated after the droplet detection from the image processing is equal to 96, 398, 624, 736, 598 and 375 droplets per cm² whereas the initial reference value of $\overline{n_{2D}}$ is equal respectively to 100, 500, 1 000, 2 000, 3 000 and 4 000 droplets per cm². Finally, dnn distributions are calculated on the whole set of the synthetic image, and the PDF and the dimensionless α_{2D}, β_{2D}, δ_{2D} and ϵ_{2D} are obtained. For the most critical case where initial $\overline{n_{2D}}$ is equal to 100 droplets per cm² and pixel size is equal to 0.1 mm, the study is carried out with around 180000 distances. According to the Figure 4, the error committed on dimensionless parameter values compared to the theoretical value is around 0.6 %, 1.5 %, 15 % and 5 % for respectively α_{3D}, β_{3D}, δ_{3D} and ϵ_{3D}. The parameter η_{2D}, which is equal to $\overline{n_{2D}}^{-\frac{1}{2}}$, is used to make the pixel size and the dnn values dimensionless. It is important to mention that the value of $\overline{n_{2D}}$ corresponds to the value obtained once the blob analysis has been performed on the synthetic image and is called in the following the "degraded droplet density number".

Figure 16 shows the evolution of the PDF for the dimensionless distance $\overline{dnn_{2D}}/\eta_{2D}$ for the initial $\overline{n_{2D}}$ equal to 250 droplets per cm² and for four dimensionless pixel size $\Delta(px)/\eta_{2D}$ values. The red line corresponds to the PDF of the 2D HC distribution function calculated with degraded $\overline{n_{2D}}$ and the blue histogram to the PDF obtained with the dnn calculated on the synthetic images.

Several conclusions can be drawn from these results. Firstly, if the dimensionless pixel size is low enough (high image resolution), the PDF of the synthetic image seems to match, visually, with the theoretical distribution (Figure 16 a and b). Secondly, increasing the dimensionless pixel size makes appear a cut-off value on the lowest values of the dnn and the values lower than $2\Delta(px)$ are no longer seen (c and d). This cut-off is explained by the artificial aggregation of the numerical droplets present in the same pixel and the artificial merging of some numerical droplets represented on different pixels but not separated by at least one pixel. Moreover, the PDF becomes less smooth. Indeed, there are some dnn which are predominant compared to other according to the theoretical HC distribution. Thirdly, this behaviour is similar for each initial $\overline{n_{2D}}$. From these observations, the PDF of the dimensionless distance $\overline{dnn_{2D}}/\eta_{2D}$ clearly depends on the dimensionless pixel size $\Delta(px)/\eta_{2D}$.

In order to highlight the influence of the image resolution on the dimensionless parameters, **Error! Reference source not found.**Figure 17 describes the evolution of α_{2D}, β_{2D}, δ_{2D} and ϵ_{2D} according to the dimensionless pixel size for several surface droplet density numbers $\overline{n_{2D}}$. The red line represents the values of the dimensionless parameter associated to the 2D Hertz-Chandrasekhar law. At first, for all the droplet density numbers, the evolution of each parameter is similar and their values are practically superimposed, thus we can assume that this evolution is universal. This implies that, for a given experimental configuration, if the surface droplet density number is known and we assume that the droplets distribution follows an Hertz-Chandrasekhar distribution, we are able to quantify the relative error for α_{2D}, β_{2D}, δ_{2D} and ϵ_{2D} values due to the image resolution. Secondly, for dimensionless pixel size values lower than 0.13, the relative errors between the simulation with synthetic image and the theoretical values are lower or around 10 % for each parameter. With the increase of the dimensionless pixel size, the absolute value of the relative errors of the parameters increase significantly at least for a certain interval. This behaviour is consistent with the visual observations on Figure 16 the previous paragraph where the theoretical and simulated PDFs are really close and then deviate more and more with the dimensionless pixel size. Thirdly, the evolution of α_{2D} and β_{2D} is monotonous according to the dimensionless pixel size in the studied interval values for dimensionless pixel size while the evolution of δ_{2D} and ϵ_{2D} is not monotonous. When $\Delta(px)/\eta_{2D}$ increases, α_{2D} increases and β_{2D} decreases. However, for a dimensionless pixel size under 0.2, δ_{2D} and ϵ_{2D} increase when $\Delta(px)/\eta_{2D}$ increases and then decreases when the dimensionless pixel size is larger than 0.2 and the value increases. For the moment, we cannot explain this observation. Finally, it is interesting to mention that when the image resolution is not sufficient according to the droplet density number then α_{2D} and δ_{2D} increase, which is a different behaviour than the one observed when there is preferential segregation effects (α decreases while δ increases). This observation can serve to determine if the deviation of the dimensionless parameters is due to only to preferential segregation effects or image resolution effect or by both simultaneously.

3.4 Application to the experimental data for the reactive case

The previous study of the experimental data for the reactive case (Rousseau et al., 2021) provides results such as the mean dnn – droplet density diagram (Figure 2 c) and the standard deviation dnn – density diagram (Figure 2 d). From these diagrams, it is observed that the droplet spatial distribution in the spray is closer to the Hertz-Chandrasekhar distribution than the simple regular grid distribution. Moreover, on the mean dnn – droplet density diagram, two regions can be observed. For surface droplet density numbers higher than 100 droplets per cm² ($\overline{n_{2D}}^{-\frac{1}{2}} < 1\,000\ \mu m$), the scatter plot is almost perfectly aligned on the random 2D HC distribution and α_{2D} is around 0.46. For surface droplet density numbers lower than 100 droplets per cm², there is a slope discontinuity where α_{2D} is around 0.36 and the cloud of points deviate slightly of the 2D HC distribution. In addition, the dispersion of the scatter plot increases in this diagram part.

In this section, we apply the results of the previous numerical study on the experimental results described above. More precisely, we try to estimate the errors committed on α_{2D} and β_{2D} values due to the experimental data acquisition and processing. From this application, we want to provide some answers to explain the difference of behaviour for the cloud of points according to the droplet density number reminded above.

Firstly, we want to estimate the errors due to the image resolution on α_{2D} and β_{2D} values, and consequently on $\overline{dnn_{2D}}$ and $\sigma_{dnn_{2D}}$. In the case under consideration, the image resolution is equal to 40 pixels per millimetre thus $\Delta(px)$ is equal to 0.025 millimetre. Figure 18**Error! Reference source not found.** shows the dimensionless pixel size map for the lower part of the combustion chamber for the reactive case. In this field, the dimensionless pixel size varies between 0.02 in the areas of lowest droplet density number and 0.12 for the areas of highest droplet density number.

From this map and Figure 17**Error! Reference source not found.**, we assume that α_{2D} value is overestimated around 6 % for the very dense regions and around 1 % for the low density regions. On the contrary, β_{2D} value is underestimated about 12 % where the droplet density number is high and around 2 % for the low droplet density number. Lastly, δ_{2D} and ϵ_{2D} are overestimated around respectively 34 % and 14 % for the very dense regions while this overestimation decreases around respectively 8 % and 5 %. In view of these results, the observed field can be separated in two areas. The first area is close to the injector and the image resolution leads to some deviations on the parameters according to the theoretical HC distribution. The second, further from the injector, where the image resolution matches with the droplet density number that implies that the value of the dimensionless parameters are not influenced by the image resolution. Consequently, the characterization of the droplet spatial distribution is more complicated for the first area than for the second area due the influence of the image resolution.

Since the slope discontinuity in the mean dnn-density diagram (Figure 2 c) appears for droplet density number lower than 100 droplets per cm² and the image resolution matches with these droplet density numbers then this discontinuity cannot be explained only by the data acquisition and processing. For this reason, the comparison of the PDF of the dimensionless distance with the 2D HC is useful to determine if this discontinuity is explained by a preferential segregation effect in the flow. To this end, three areas of the lower part of the combustion chamber with different values of the surface droplet density number have been studied (Figure 19 a). In the first two areas, $\overline{n_{2D}}$ is higher than 100 droplets per cm² while the third $\overline{n_{2D}}$ is lower. The number of droplets contained in each area are around 818 000, 988 000 and 142 000 respectively for zone 1, zone 2 and zone 3

In the first and second areas, a cut-off is observed for the lower values of the dimensionless distance. It can be explained by the image resolution that is not sufficient according to the droplet density number and leads to an artificial merging of droplets (see section 3.3). For $\frac{\overline{dnn_{2D}}}{\eta_{2D}}$ values higher than this cut-off, the histograms are close to the 2D HC distribution. On the contrary, for the third area, there is a small cut-off but the PDF is shifted towards the lowest values of $\frac{\overline{dnn_{2D}}}{\eta_{2D}}$ which reflects the presence of preferential segregation in this area according to the conclusions of the section 3.1.1.

From these observations, there are two distinguishable areas in the spray for the lower part of the combustion chamber.

The first one is located close to the injector and extends from X included between 10 mm and 50 mm and Y included between 30 mm and 60 mm. This area is represented on the mean dnn-density diagram by the cloud of points close to the 2D HC distribution and where the global α_{2D} value deduced from all these points is equal to 0.46. Nevertheless, since the droplet

density number varies significantly (from around 200 droplets per cm² and 2500 droplets per cm²) then the dimensionless pixel size varies too and locally the α_{2D} value, and consequently $\overline{dnn_{2D}}$, are overestimated by about 2 % to 6 %. Therefore, it can be possible to estimate the global α_{2D} value around 0.43 and 0.45. Moreover, the study of the dnn histograms in this area shows that, despite a cut-off for the lowest value of dnn, shows that dnn histograms are close to the 2D HC distribution. The combination of these two observations leads to think that the droplet spatial distribution in this area is close to the HC distribution even if the characterization is not complete due to the poot image resolution according to the droplet density number. In the section 3.2.1, we have shown that the transition from a 3D field where droplets are distributed according to the 3D HC law gives a 2D field where spatial droplet distribution follows the 2D HC law, and conversely. Thus, we can assume that inside the combustion chamber and in this first area, the droplets are distributed according to the 3D HC distribution.

The second area is located far away from the injector and is represented on the mean dnn-density diagram by the cloud of points which deviate from the 2D HC distribution. The global α_{2D} value deduced from all these points is equal to 0.36 and the image resolution matches with the droplet density number in this area which means that this estimation is accurate. This deviation of α_{2D} value is consistent with the dnn histogram in this area which shows that preferential segregation effects occur. We can assume that the combustion phenomenon has an influence on the droplet spatial distribution and leads to the preferential segregation droplet distribution. The group combustion theory (Chiu et al., 1977) could explain partially the preferential segregation effect since the "internal group combustion", the "external group combustion" and the "external sheath combustion" are configurations where droplets burn together.

4 Conclusion

This paper proposes a study in order to better understand how characterize droplet spatial distribution from experimental data and especially Mie scattering images.

To this end, we compare firstly the first four moments of the PDF α, β, δ and ϵ (resp. mean, standard deviation, skewness and kurtosis) associated to the droplet spatial distribution for the cases of the Hertz-Chandrasekhar, the preferential segregation and the inhomogeneous Poisson distributions. In presence of a preferential segregation or on inhomogeneous Poisson distribution, the values of the moments deviate from their theoretical values based on the Hertz-Chandrasekhar distribution. More precisely, the mean value α is lower than its theoretical value while the other three values are greater. Such a feature could be helpful to distinguish between the distributions observed experimentally or numerically.

Secondly, the study of the 3D-2D transition process shows that the transition from a 3-dimensional droplet field to its 2-dimensional projection images generates a restriction error and a projection bias. The first one is due to the transition from a 3D cubic droplet field to a 3D slice representative of the laser sheet. The second one is due to the projection of this slice on a 2D surface representative of experimental images. The errors depend on the combination of the slice thickness and the droplet density number. Moreover, it is shown that the projection of a 3D droplet field obeying to the 3D Hertz-Chandrasekhar distribution leads to a 2D droplet field obeying to the 2D Hertz-Chandrasekhar distribution. Finally, in order to recreate a 3D droplet field from a 2D droplet field, a relationship for the estimation of the relative difference between $\overline{dnn_{3D}}$ and $\overline{dnn_{2D}}$ which takes into account the slice thickness e, the surface droplet density

number $\overline{n_{2D}}$ and the ratio between α_{2D} and α_{3D} is proposed. When the two parameters are fixed by the 2D droplet field for any case, the ratio α_{2D}/α_{3D} depends on the distribution. For a Hertz-Chandrasekhar distribution, this ratio equals to the ratio of the theoretical values respectively for 2D and 3D Hertz-Chandrasekhar distribution. For the preferential segregation distribution, this ratio depends on the Stokes number and the ratio of the dimensionless slice thickness e/η_{2D}. It could be interesting that this relationship would be modelled in further works.

Thirdly, the study about the influence of the image resolution on the characterization of the spatial droplet distribution shows that a poor image resolution according to the droplet density number leads to a deviation of the first four moments of the PDF. When the image resolution is degraded then α, δ and ϵ values increase while β value decreases. Furthermore, a cut-off value on the lowest values of the dnn appears which is due to the poor resolution of the image and the algorithmic process (merging of the droplets).

Finally, the end of the paper is dedicated to the application of the previous conclusion to experimental data obtained under reactive conditions from the Mie scattering images acquired. It is found that the observed field is constituted of two areas. The first area is close to the injector and the image resolution is not sufficient according to the droplet density number. Thus, analysing the droplet spatial distribution is not obvious. However, that may be a droplet spatial distribution which seems close to the Hertz-Chandrasekhar distribution. Far away from the injector, the image resolution matches the droplet density number and the deviation of the PDF shows the spatial droplet distribution involves preferential segregation effects.

Appendix

Ten samplings of the Monte-Carlo simulation for the configuration of 50 000 droplets in the computational volume, a droplet density number $\overline{n_{3D}}$ equals to 100 droplets per cm^{-3} and a dimensionless size of the computational volume L/η_{3D} equals to 37 have been carried out. Figure 20 shows the relative error on the dimensionless parameters α_{3D}, β_{3D}, δ_{3D} and ϵ_{3D} for each draw. The symbols correspond to the relative error value for each draw and the solid red line corresponds to the mean value of the relative error. This figure shows that, for each dimensionless parameters, the value of the relative error fluctuates around a mean value. However, this variation is marginal for α_{3D} and β_{3D} while it is more important for δ_{3D} and ϵ_{3D}.

Reference

Abramzon B, Sirignano WA (1989) *Droplet vaporization model for spray combustion calculations.* International Journal of Heat Mass Transfert 32(9):1605-1618
https://doi.org/10.1016/0017-9310(89)90043-4

Boutsikakis, A. (2020). *Numerical simulation and physical analysis of the dispersion of charged inertial particles transported by stationary homogeneous isotropic turbulence*. PhD Thesis, IMFT

Chandrasekhar S (1943) *Stochastic problems in physics and astronomy*. Rev. Mod. Phys. Vol. 15, Iss. 1
https://doi.org/10.1103/RevModPhys.15.1

Chauveau C, Halter F, Gökalm I (2006) *Vaporization in three-dimensional droplet arrays: effects of the fuel vapour saturation*. ICLASS-2006, Kyoto, Japan. Paper ID ICLASS06-229

Chen G, Gomez A (1997) *Dilute laminar spray diffusion flames near the transition form group combustion to individual droplet burning*. Combustion Flame 110:392-404
https://doi.org/10.1016/S0010-2180(97)00087-4

Chiu HH, Liu TM (1977) G*roup combustion of liquid droplets*. Combustion Flame 17:127-142
https://doi.org/10.1016/S0082-0784(82)80273-7

Chiu HH, Kim HY, Croke EJ (1982) *Internal group combustion of liquid droplets. 19th symposium international on combustion*. Combustion Institute 19:971-980
https://doi.org/10.1016/S0082-0784(82)80273-7

Fede P, Simonin O, Villedieu P (2015) *Monte-Carlo simulation of colliding particles or coalescing droplets transported by a turbulent flow in the framework of a joint fluid-particle pdf approach*. International Journal of Multiphase Flow 74 (0):165-183
https://doi.org/10.1016/j.ijmultiphaseflow.2015.04.006

Février P, Simonin O, Legendre D (2001) *Particle dispersion and preferential concentration dependance on turbulent Reynolds number from direct numerical simulation and large eddy simylation of isotropic homogeneous turbulence*. Proceeding of the 4th international conference on multiphase Flow, New Orleans, USA.

Godsave GAE (1953) *Studies of the combustion of drops in a fuel spray: the burning of a single droplet of fuel. 4th symposium international on combustion*. Combustion Institute 4:818-830

Hertz P (1909) *Uber den gegenseitigen durchsnittlichen Abstand Von Punkten, die mit bekannter mittlerer Dichte im Raume angeordnet sind*. Math. Ann 67(3):387-398

Imaoka RT, Sirignano WA (2005) *Vaporization and combustion in a three-dimensional droplet arrays*. Combustion Institute 30:1981-1989
https://doi.org/10.1016/j.proci.2004.08.049

Jiang TL, Chen WH, Tsai MJ, Chiu HH (1995) *A numerical investigation of multiple flame configurations in convective droplet gasification*. Combustion Flame 3:221-238
https://doi.org/10.1016/0010-2180(95)92244-2

Kerstein AR, Law CK (1982) *Percolation in combustion spray I: transition from cluster combustion to percolate combustion in non-premixed sprays*. Combustion Institute 19:961-969
https://doi.org/10.1016/S0082-0784(82)80272-5

Kostinski AB, Shaw RA (2001) *Scale-dependent droplet clustering in turbulent clouds*. Journal of Fluid Mechanics 434:389-398
https://doi.org/10.1017/S0022112001004001

Laboswki M (1976) *The effects of nearest neighbour interactions on the evaporation rate of cloud particles.* Chemical Engineering Science 33:803-813
https://doi.org/10.1016/0009-2509(76)80054-1

Li SC, Libby PA, Williams FA (1993) *Spray structure in counterflowing streams with and without a flame*. Combustion Flame 94:161-177
https://doi.org/10.1016/0010-2180(93)90028-2

Lumley JL (1970) *Stochastic tools in turbulence*. Applied Mathematics and mechanics. Vol. 12

Mikami M, Mizuta Y, Tsuchida Y, Kojima N (2009) *Flame structure and stabilization of lean-premixed sprays in a counterflow with low-volatility fuel*. Combustion Institute 32:2223-2230
https://doi.org/10.1016/j.proci.2008.08.009

Milchev A (1994) *On the spatial and temporal distribution of clusters*. Journal of Chemical Physics 100,5160
https://doi.org/10.1063/1.467180

Orain M, Mercier X, Grisch F (2005) *PLIF imaging of fuel vapour spatial distribution in an acetone droplet stream, comparison with modeling*. Journal of Combustion Science Technology 177:249-278
https://doi.org/10.1080/00102200590900228

Paulhiac D (2015) *Modélisation de la combustion d'un spray dans un brûleur aéronautique*. PhD Thesis, INP Toulouse

Réveillon J, Vervisch L (2005) *Analysis of weakly turbulent dilute-spray flames and spray combustion regimes*. Journal of Fluid Mechanics 537:317-347
https://doi.org/10.1017/S0022112005005227

Rousseau L, Lempereur C, Orain M, Rouzaud O, Simonin O (2021) *Droplet spatial distribution in a spray under evaporating and reacting conditions.* Experiments In Fluids, 62 (26). ISSN 0723-4864
https://doi.org/10.1007/s00348-020-03129-9

Rouzaud O, Vicentini M, Lecourt R, Bodoc V, Simonin O (2016) *Experimental analysis of droplet spatial distribution in a spray burner*. 27th ILASS Conference

Rouzaud O, Vicentini M, Lecourt R, Simonin O, Bodoc V, Fede P (2021) *Experimental analysis of droplet spatial distribution in a spray burner*. Atomization and Spray, 31 (6). 1-22 ISSN 1044-5110
https://doi.org/10.1615/AtomizSpr.2021034211

Sahu S, Hardalupas Y, Taylor AMKP (2014) *Droplet-turbulence interaction in a confined polydispersed spray: effect of droplet size and flow length scales on spatial droplet-gas velocity correlations*. Journal of Fluid Mechanics 741:98-138
https://doi.org/10.1017/jfm.2013.676

Sahu S, Hardalupas Y, Taylor AMKP (2016) *Droplet-turbulence interaction in a confined polydispersed spray: effect of turbulence on droplet dispersion*. Journal of Fluid Mechanics 794:267-309
https://doi.org/10.1017/jfm.2016.169

Sahu S, Hardalupas Y, Taylor AMKP (2018) *Interaction of droplet dispersion and evaporation in a polydispersed spray*. Journal of Fluid Mechanics 846:37-81
https://doi.org/10.1017/jfm.2018.247

Silverman MA, Dunn-Rankin D (1994) *Experimental investigation of a rectilinear droplet stream flame*. Journal of Combustion Science Technology 100:57-73
https://doi.org/10.1080/00102209408935446

Sirignano WA (2014) *Advances in droplet array combustion theory and modelling*. Progress In Energy and Combustion Science 42:54-86
https://doi.org/10.1016/j.pecs.2014.01.002

Shanbhogue SS, Husain S, Lieuwen T (2009) Lean blowoff of bluff body stabilized flames : scaling and dynamics. Progress in Energy and Combustion Science. 35:98-120
https://doi.org/10.1016/j.pecs.2008.07.003

Shaw RA, Kostinski AB, Larsen ML (2002). *Towards quantifying droplet clustering in clouds*. Quartely Journal of the Meteorological Society, Vol. 128, No 582
https://doi.org/10.1256/003590002320373193

Spalding DB (1953) *The combustion of liquid fuels*. Combustion Institute 4:847-864

Squires KD, Eaton JK (1991) *Preferential concentration of particles by turbulence*. Physics of Fluids A 3:1169
https://doi.org/10.1063/1.858045

Suzuki I., Chiu HH (1971) *Multi-droplet combustion of liquid propellants*. 9th International Symposium on Space Technology and Science, p.145

Vicentini M (2016) *Mise en évidence expérimentale et modélisation des régimes de combustion diphasique présents dans les foyers aéronautiques*. PhD Thesis, ONERA

Williams A (1973) *Combustion of droplets of liquid fuels: a review*. Combustion Flame 21:1-31
https://doi.org/10.1016/0010-2180(73)90002-3

Figures

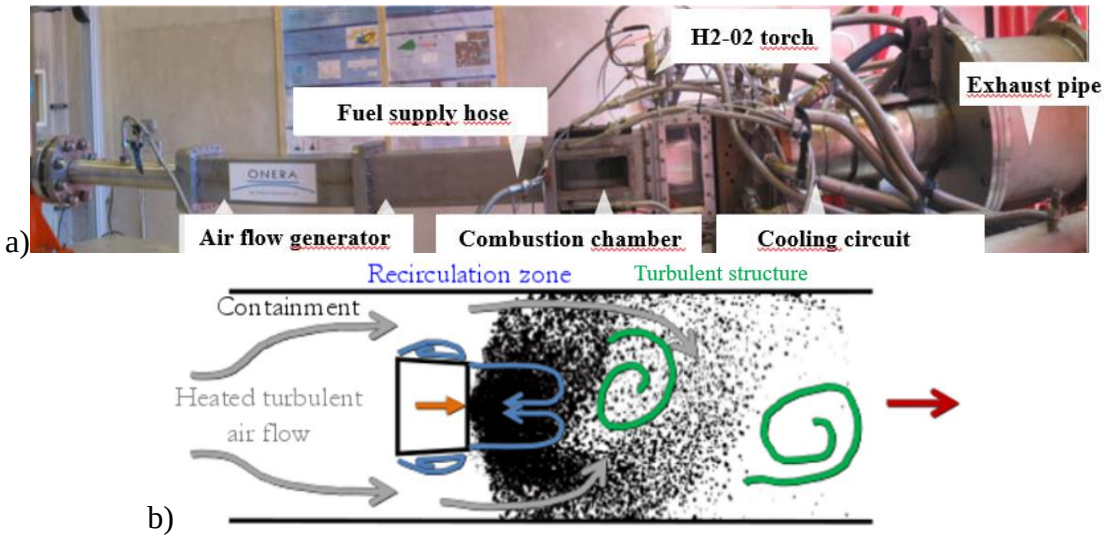

Figure 1 : General description of the test rig a) View of the LACOM device and PROMETHEE test rig b) Sketch of the flow under non-reacting conditions

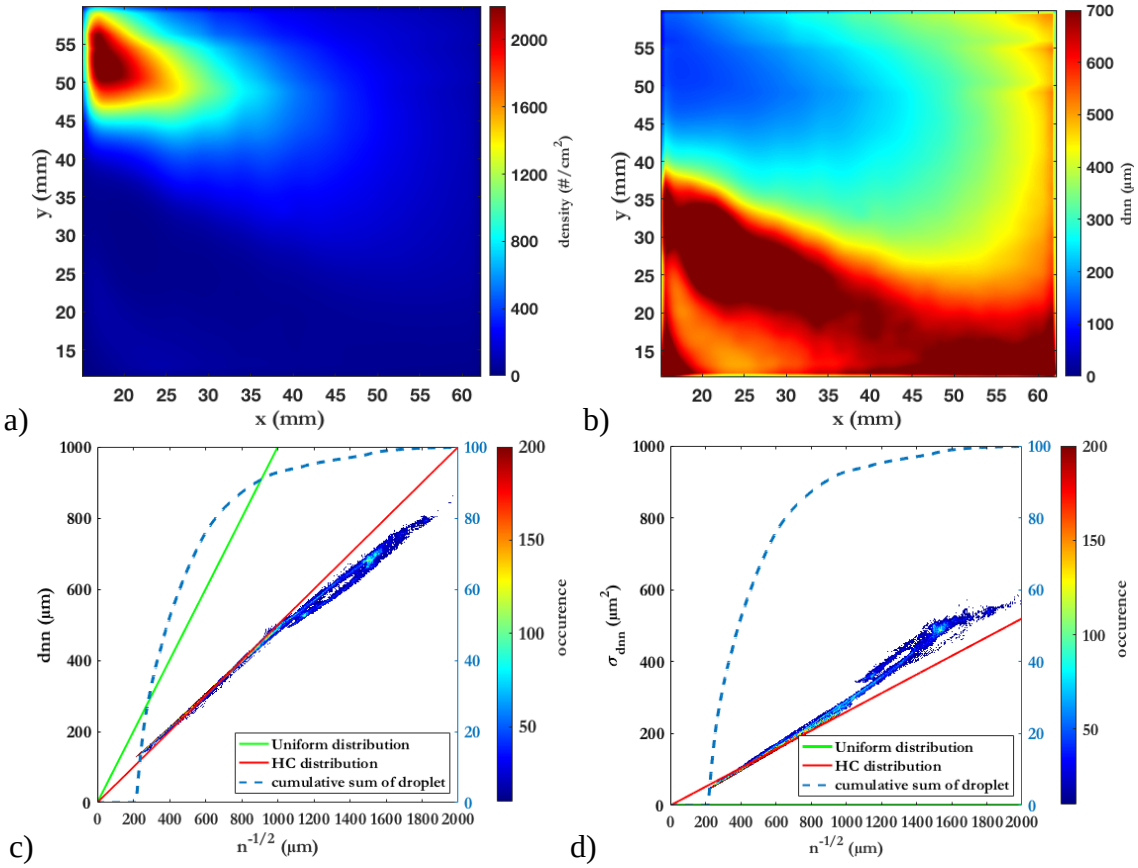

Figure 2 : In the case of reacting conditions for the lower part of the combustion chamber a) mean droplet density number map b) mean dnn map c) mean dnn – droplet density number diagram and d) standard deviation dnn – droplet density number diagram

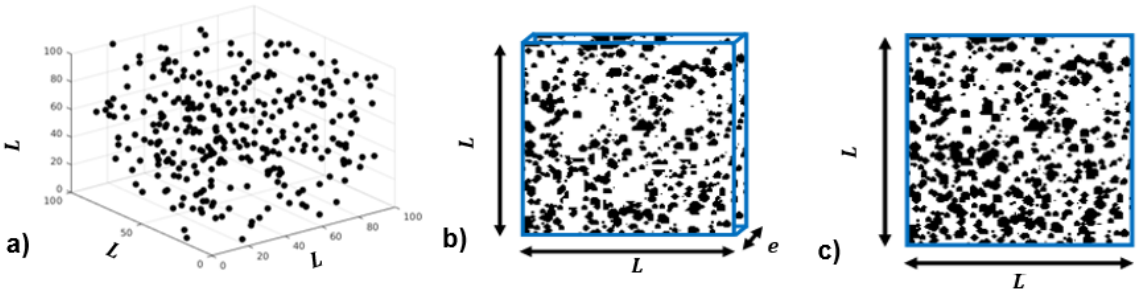

Figure 3: transition steps from the 3D data to the 2D data

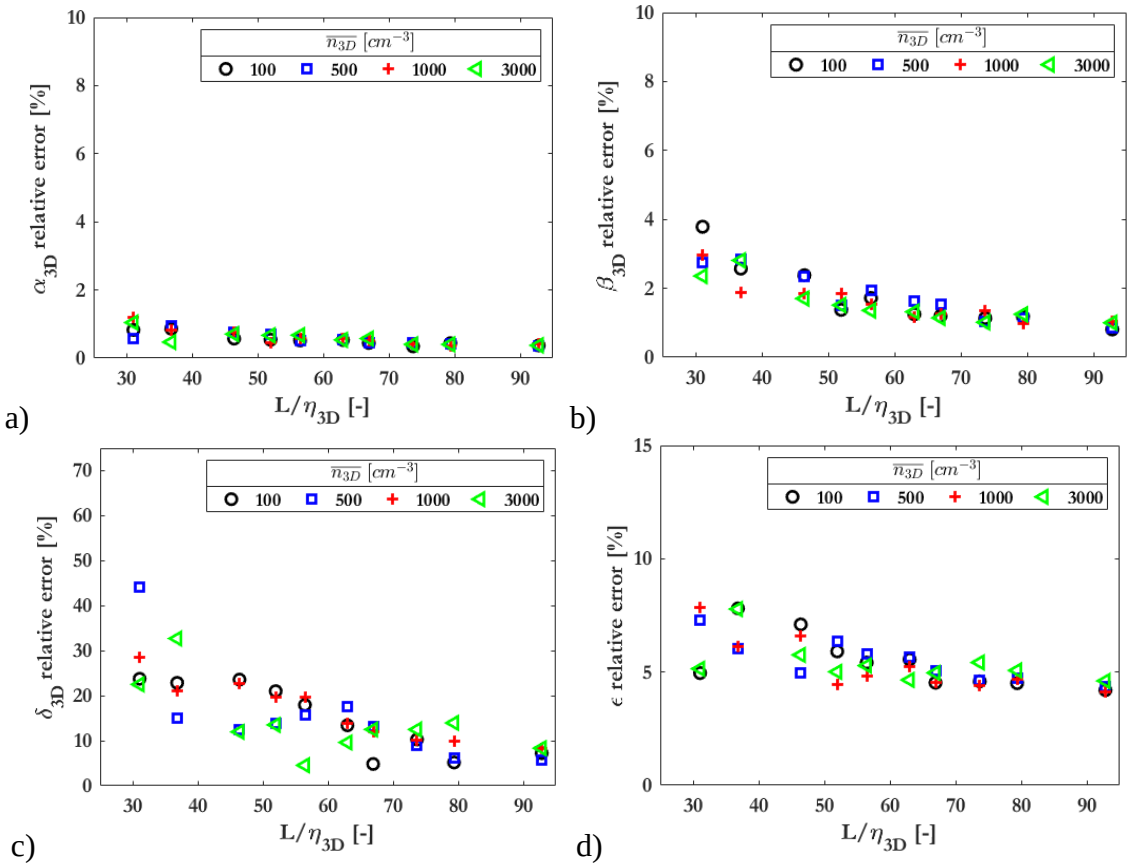

Figure 4 : Evolution of the relative error for the a) 3D dimensionless mean b) 3D dimensionless standard deviation c) 3D skewness and d) 3D kurtosis according to the dimensionless cube size for the Monte-Carlo approach

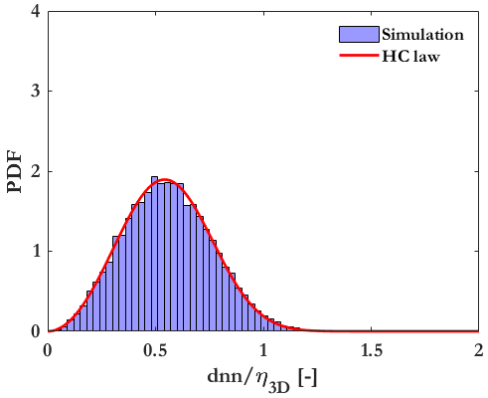

Figure 5 : Comparison of the pdf between the theoretical case (red line) and the Monte-Carlo simulation (blue) for the case of $\overline{n_{3D}}$ equals to 1000 droplet per cm^3 and L/η_{3D} equals to 56

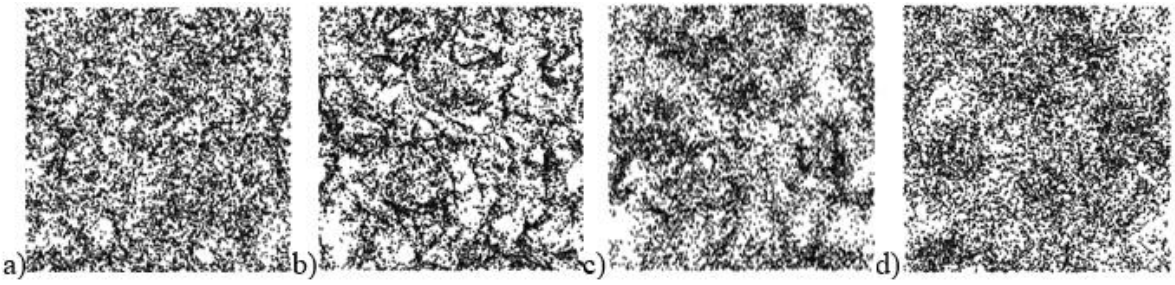

Figure 6 : Visualizations of droplets spatial distribution a) St = 0.33 b) St = 1.37 c) St = 5.06 d) = 14.42

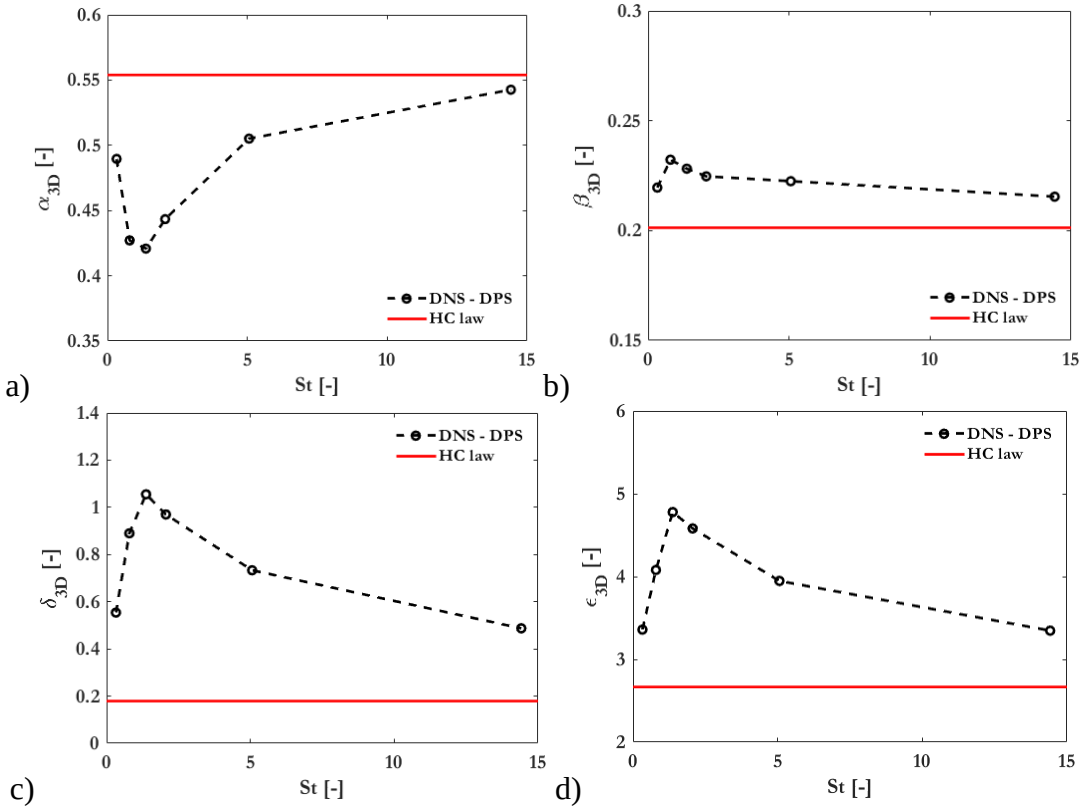

Figure 7 : Evolution of a) dimensionless mean b) dimensionless standard deviation c) dimensionless skewness and d) dimensionless kurtosis according to the Stokes number for DNS – DPS simulations

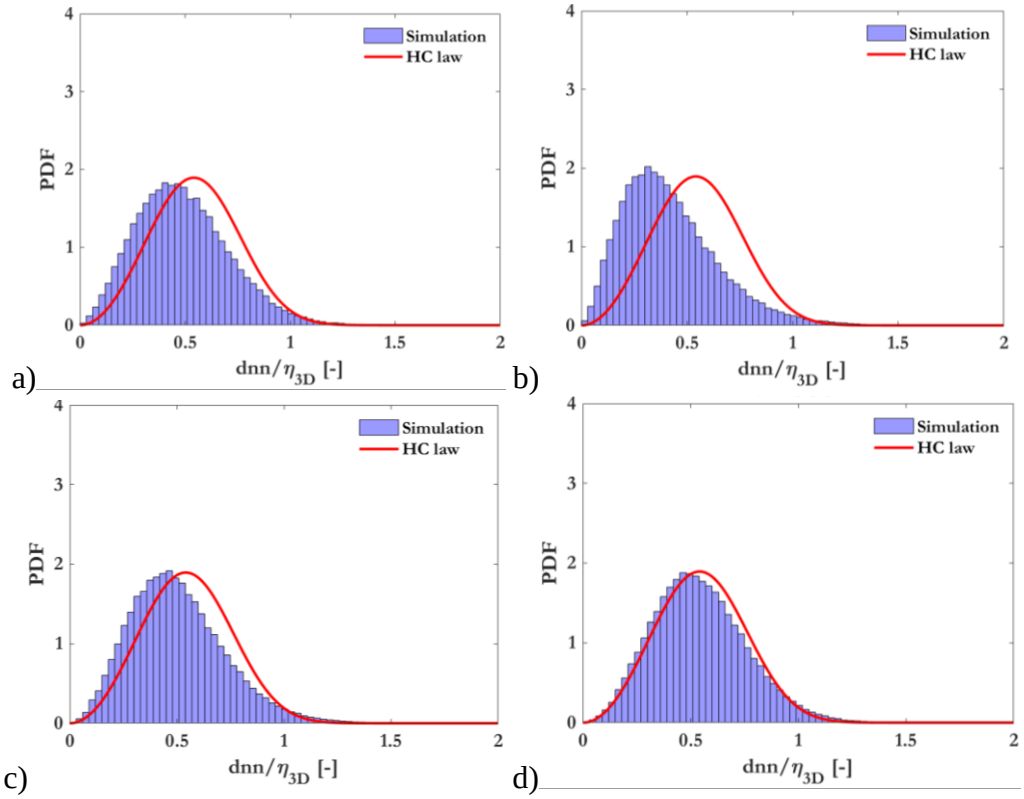

Figure 8 : Comparison between Hertz – Chandrasekhar distribution PDF and distribution with preferential segregation PDF for a) St = 0.32 b) St = 1.37 c) St = 5.06 and d) St = 14.41

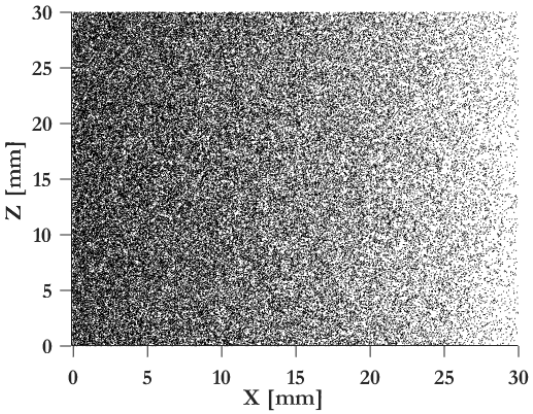

Figure 9 : Droplets distribution in a Y-plane with a density gradient

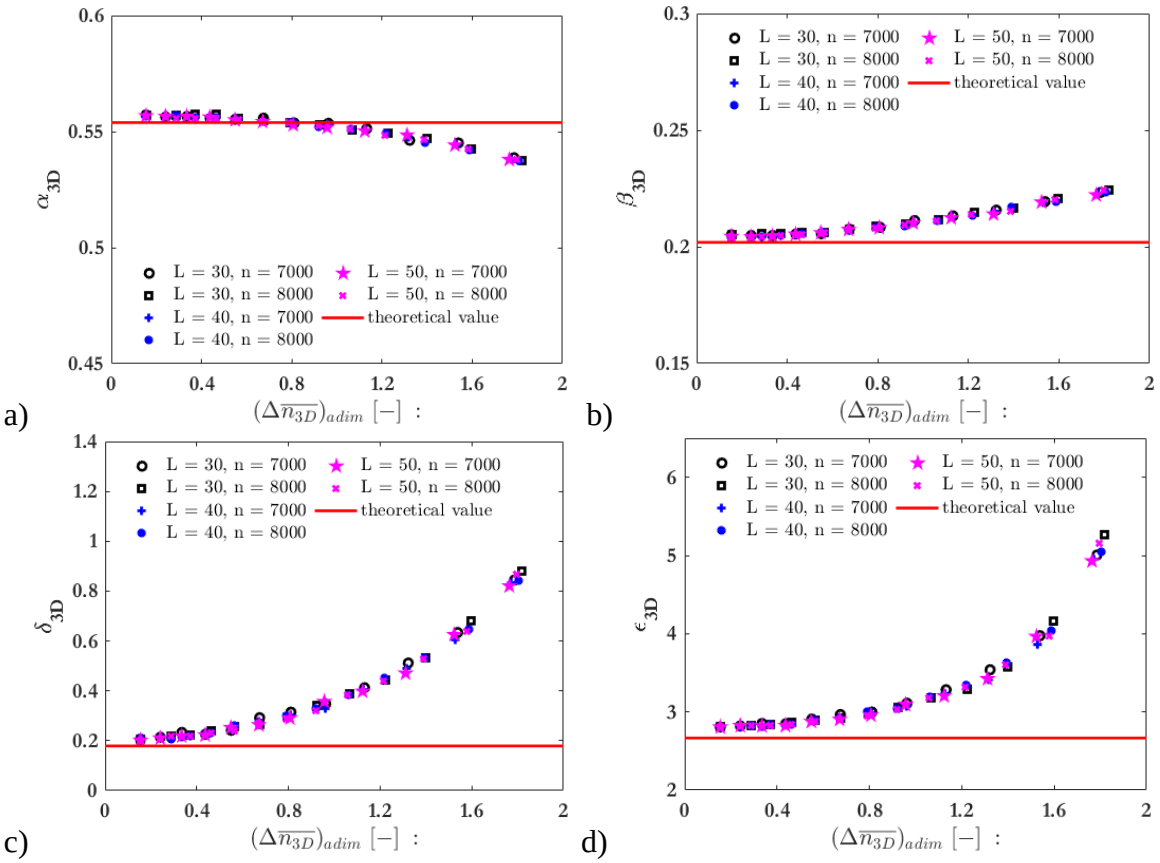

Figure 10 : Evolution of the a) dimensionless mean b) dimensionless standard deviation c) dimensionless skewness and d) dimensionless kurtosis according to the mean dimensionless 3D density gradient

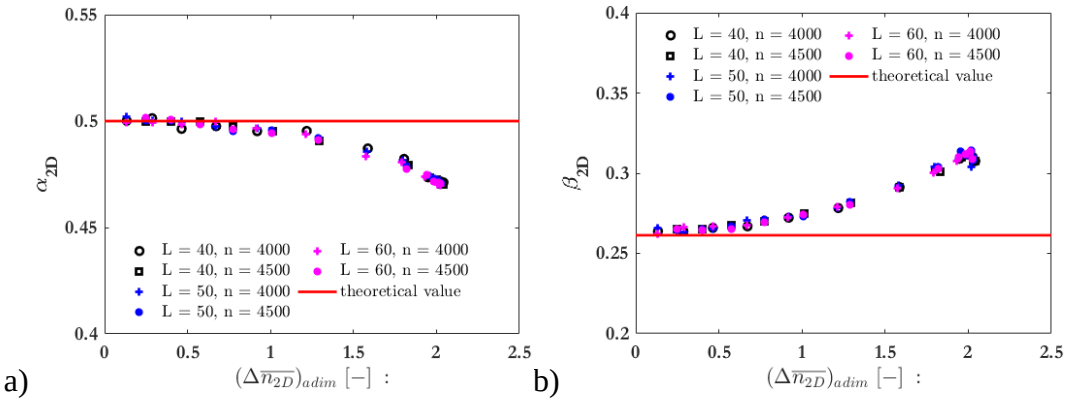

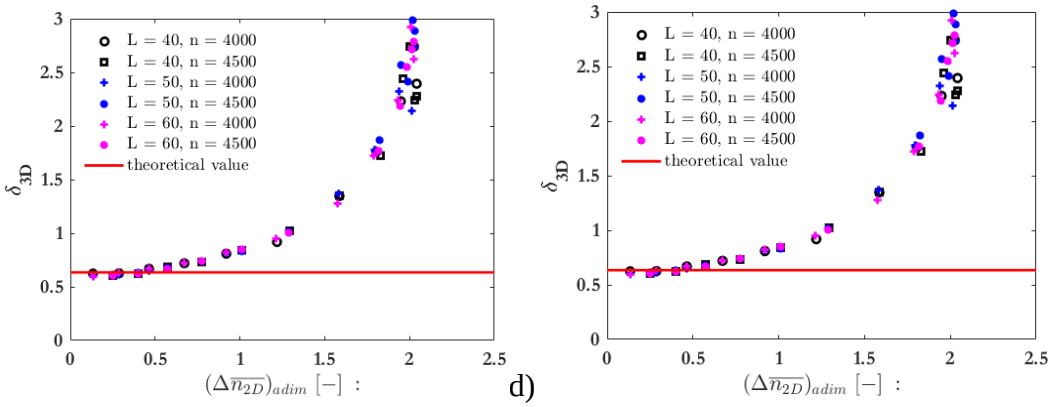

Figure 11 : Evolution of the a) dimensionless mean b) dimensionless standard deviation c) dimensionless skewness and d) dimensionless kurtosis according to the mean dimensionless 2D density gradient

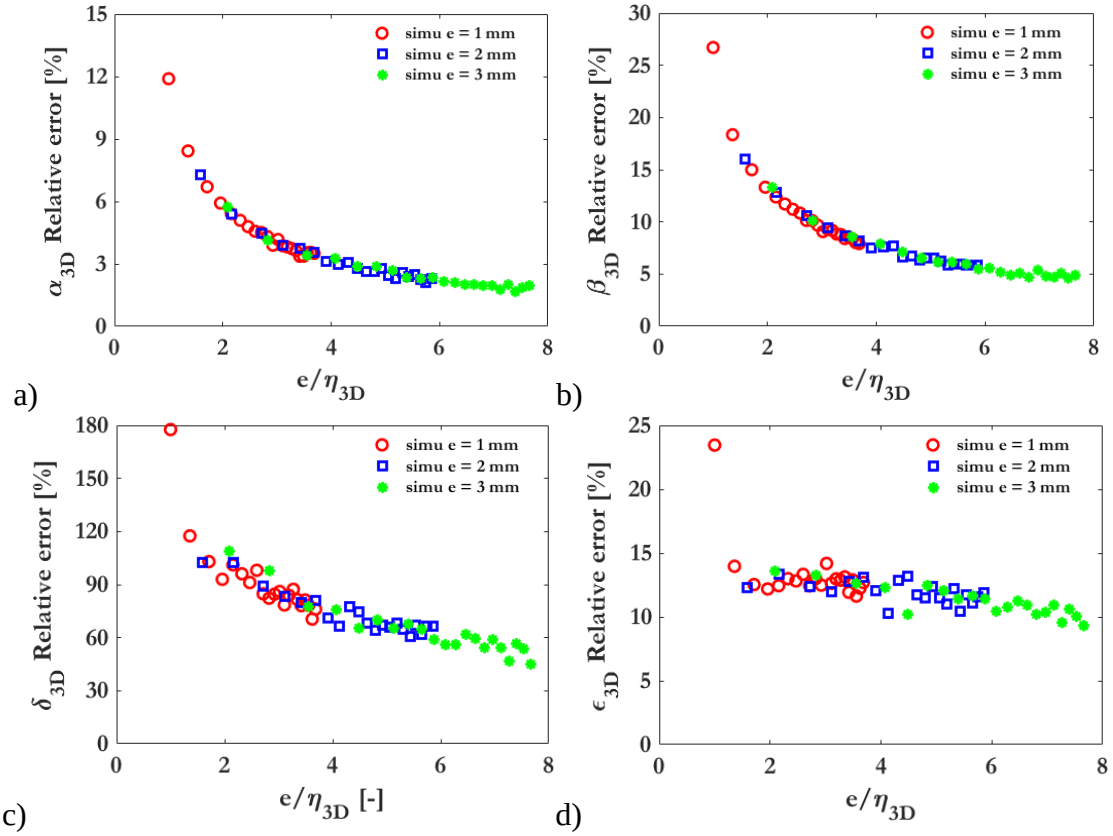

Figure 12 : Evolution of the relative error due to the restriction effect for a) 3D dimensionless mean b) 3D dimensionless standard deviation c) 3D dimensionless skewness and d) 3D dimensionless kurtosis according to the dimensionless thickness

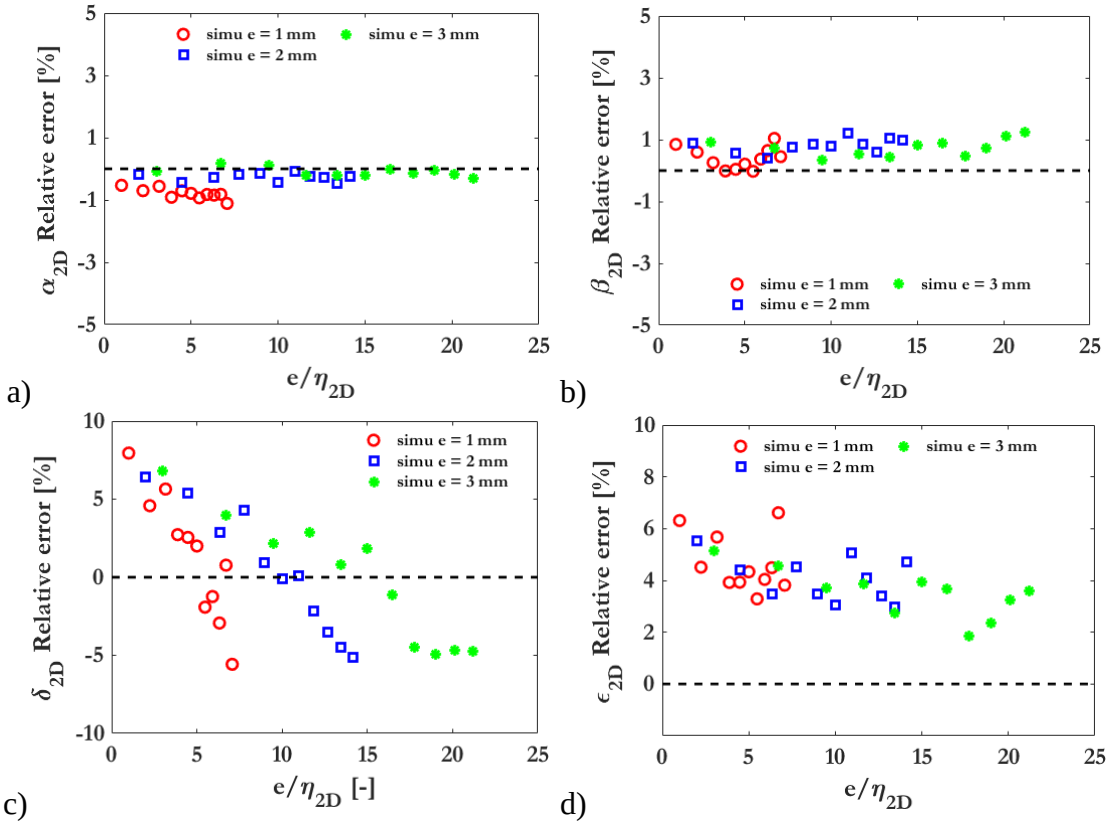

Figure 13: Evolution of the relative error for a) 2D dimensionless mean b) 2D dimensionless standard deviation c) 2D dimensionless skewness and d) 2D dimensionless kurtosis according to the dimensionless thickness

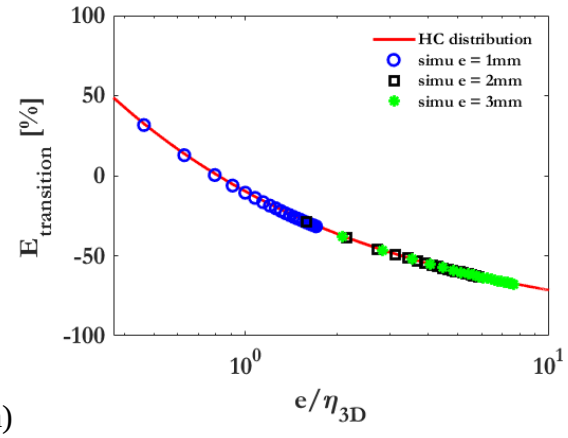

Figure 14: Evolution of the relative difference between $\overline{n_{3D}}$ and $\overline{n_{2D}}$ after the 3D-2D transition according to the dimensionless thickness

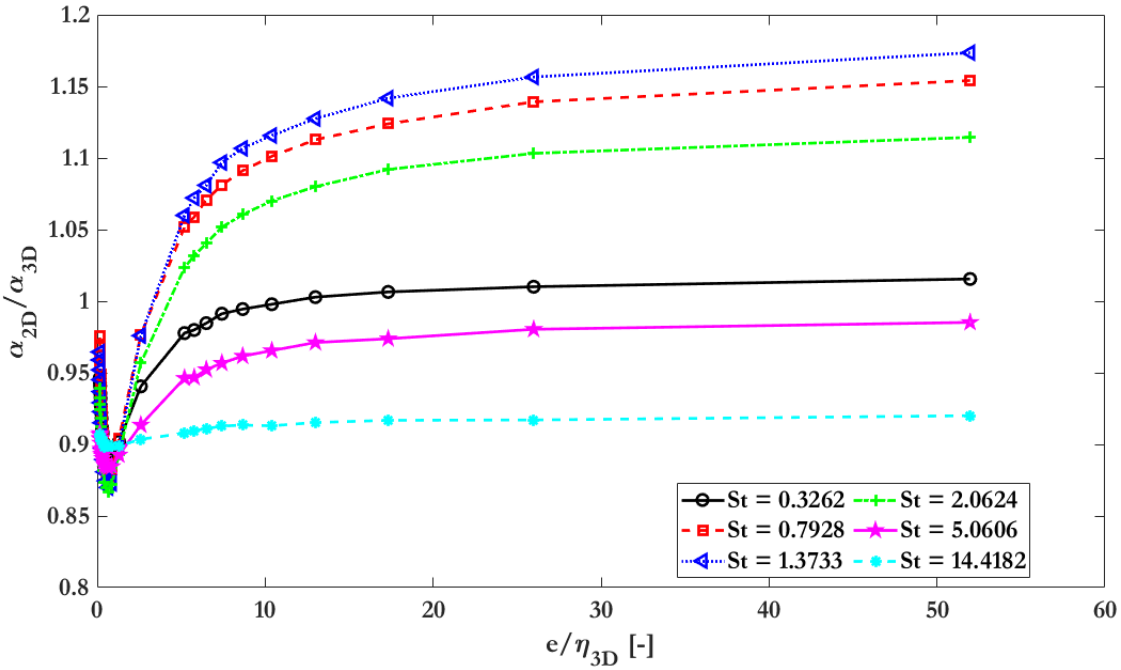

Figure 15 : Evolution of the ratio of 2D dimensionless mean to 3D dimensionless mean according to the dimensionless thickness and the Stokes number

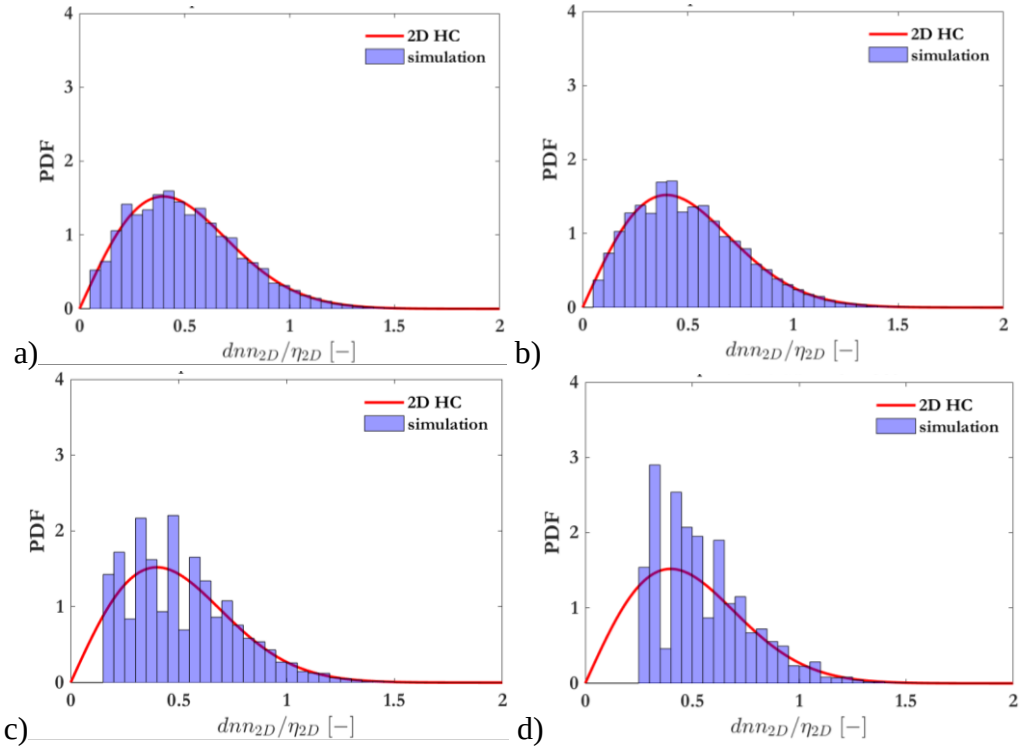

Figure 16 : PDF of the dnn in 2D for initial $\overline{n_{2D}}$ equals to 250 droplets per cm² according to the dimensionless pixel size for a) $\frac{\Delta(px)}{\eta_{2D}} = 0.026$ b) $\frac{\Delta(px)}{\eta_{2D}} = 0.039$ c) $\frac{\Delta(px)}{\eta_{2D}} = 0.077$ d) $\frac{\Delta(px)}{\eta_{2D}} = 0.149$

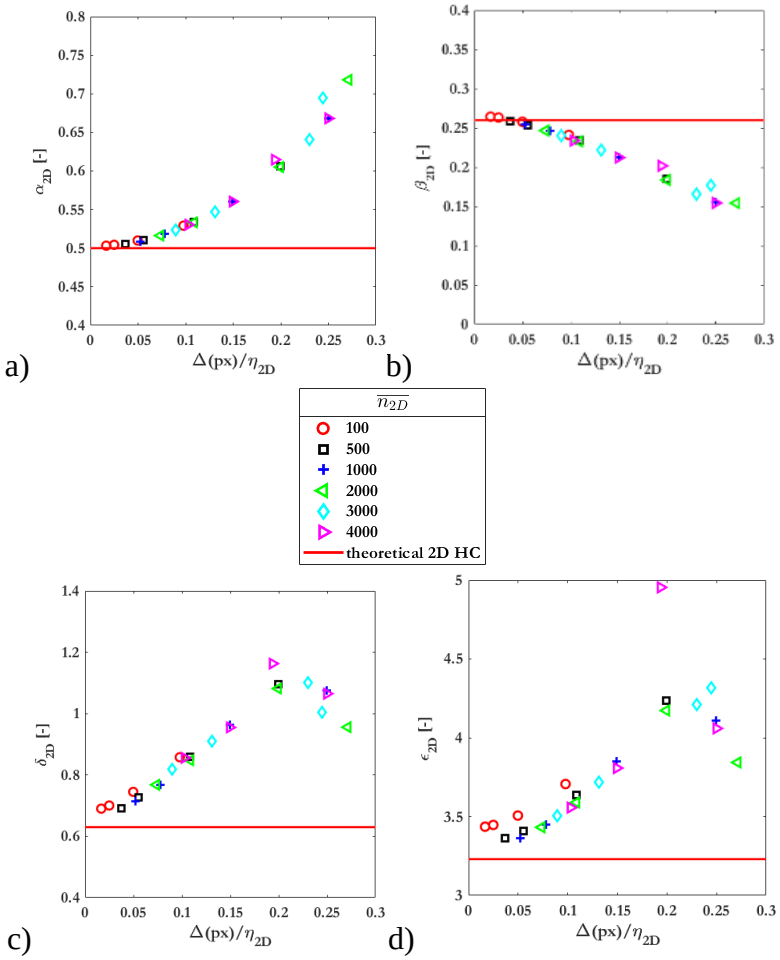

Figure 17: Evolution of a) dimensionless mean b) dimensionless standard deviation c) dimensionless skewness and d) dimensionless kurtosis according to the dimensionless pixel size

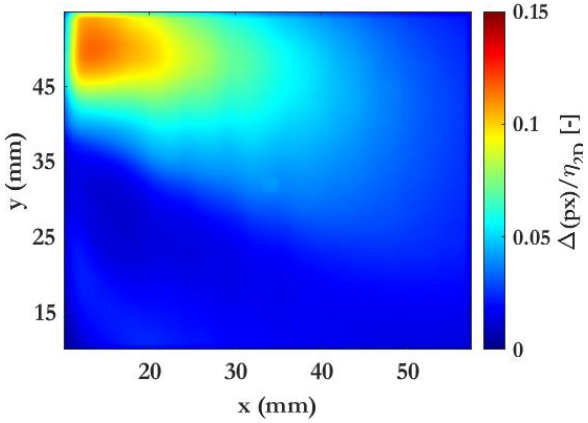

Figure 18 : Dimensionless pixel size map in the case of reacting conditions for the lower part of the combustion chamber. The image resolution is around 40 pixels per millimetres

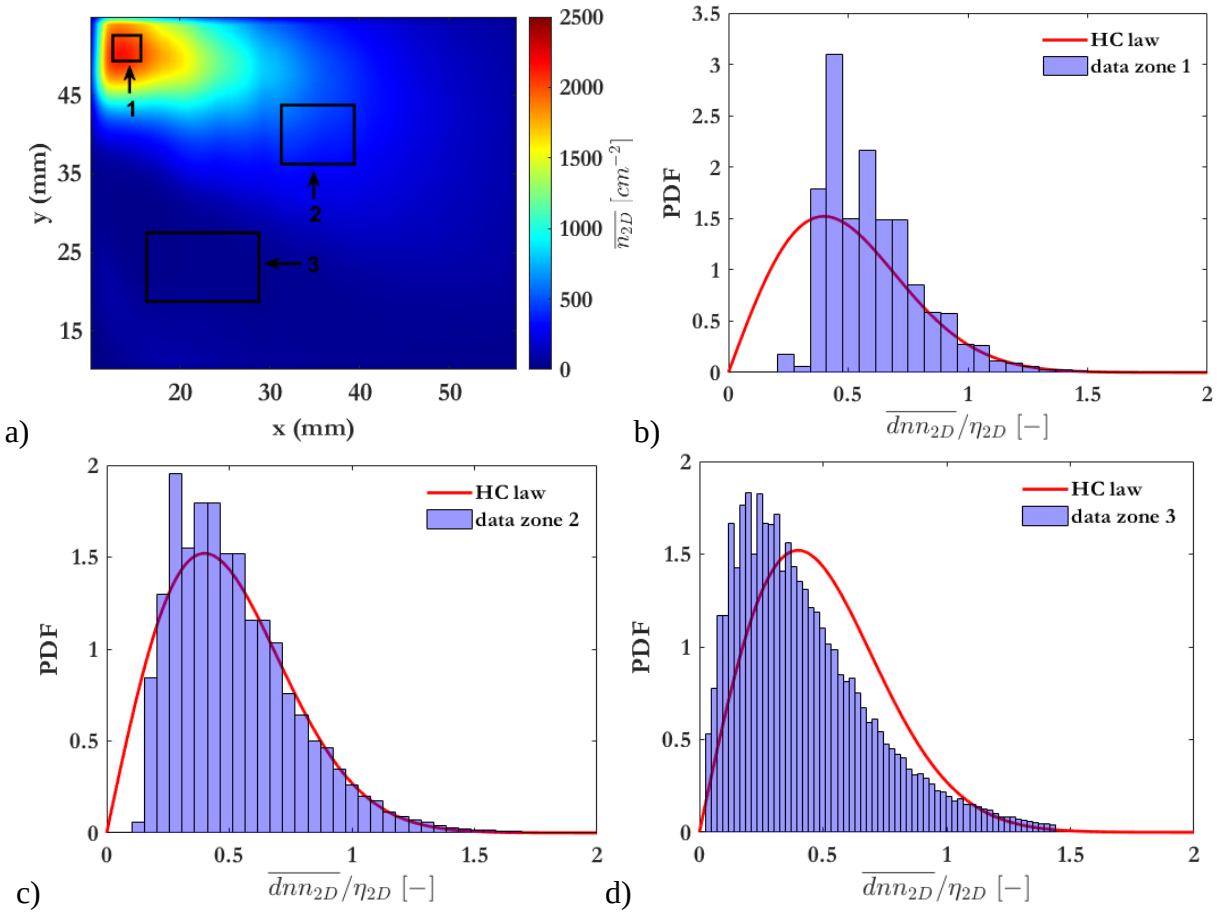

Figure 19 : a) Map of the location of the studied areas b) dimensionless distance PDF for the zone 1 where the surface droplet density number is high b) dimensionless distance PDF for the zone 2 where the surface droplet density number is medium d)) dimensionless distance PDF for the zone 3 where the surface droplet density is low

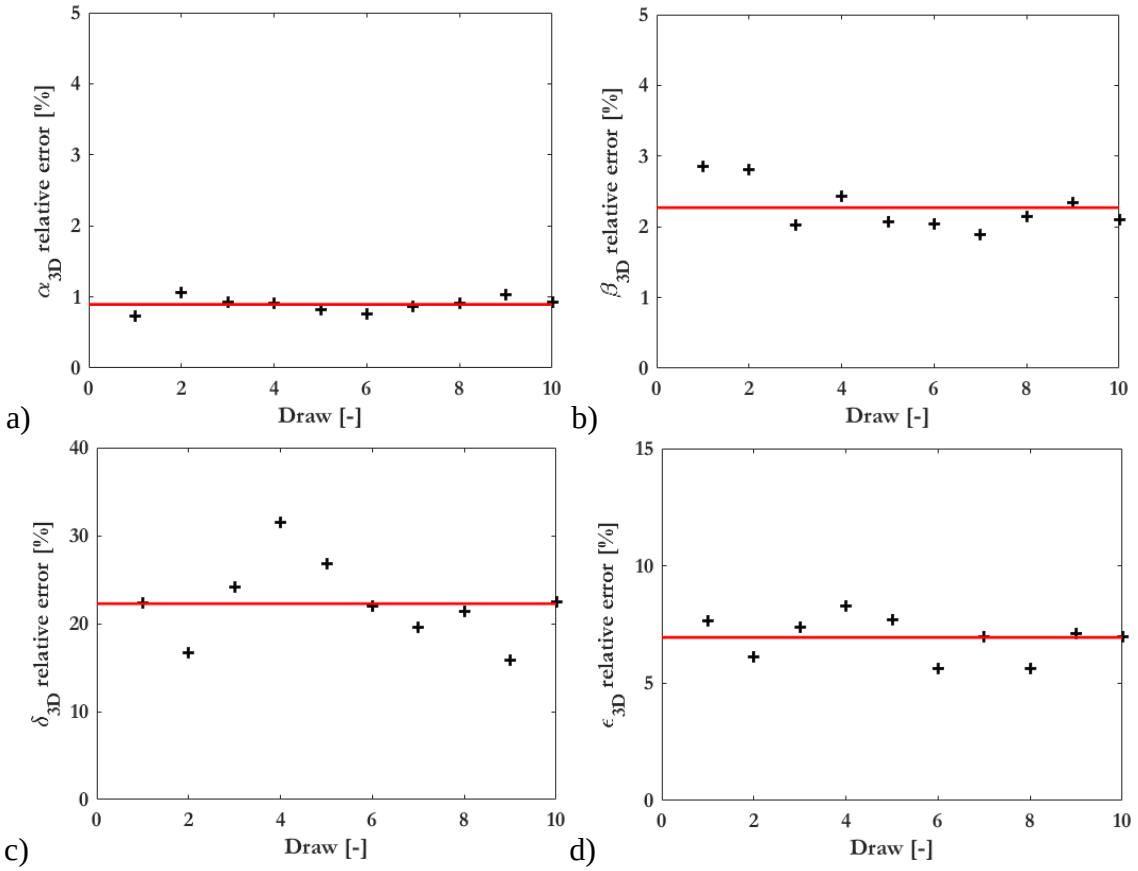

Figure 20 : Evolution of the relative error for the a) 3D dimensionless mean b) 3D dimensionless standard deviation c) 3D skewness and d) 3D kurtosis according to the draw Monte-Carlo simulation for the case of 50 000 droplets in the computational volume, $\overline{n_{3D}}$ equals 100 droplets per cm^{-3} and L/η_{3D} equals to 37

Tables

Configuration	L [mm]	$\overline{n_{max}}$ $[droplets.cm^{-3}]$	$\overline{n_{min}}$ $[droplets.cm^{-3}]$
1	30	7000	500 : 500 : 6000
2	30	8000	500 : 500 : 6000
3	40	7000	500 : 500 : 6000
4	40	8000	500 : 500 : 6000
5	50	7000	500 : 500 : 6000
6	50	8000	500 : 500 : 6000

Table 1 : Sum up of the different test configuration for the 3D droplet density gradient study

Configuration	L $[mm]$	$\overline{n_{max}}$ $[droplets.cm^{-2}]$	$\overline{n_{min}}$ $[droplets.cm^{-2}]$
1	40	4 000	[10;25;50;100;250;500 : 500 : 3 500]
2	40	4 500	[10;25;50;100;250;500 : 500 : 3 500]
3	50	4 000	[10;25;50;100;250;500 : 500 : 3 500]
4	50	4 500	[10;25;50;100;250;500 : 500 : 3 500]
5	60	4 000	[10;25;50;100;250;500 : 500 : 3 500]
6	60	4 500	[10;25;50;100;250;500 : 500 : 3 500]

Table 2 : Sum up of the different test configuration for the 2D droplet density gradient study

$\Delta(px)$ $[mm]$ / $\overline{n_{2D}}$ $[cm^{-2}]$	**0.1**	**0.05**	**0.025**	**0.0167**
100	0.5	0.12	0.03	0.03
500	2.45	0.60	0.15	0.15
1 000	4.84	1.24	0.31	0.31
2 000	9.38	2.47	0.62	0.62
3 000	13.64	3.66	0.94	0.94
4 000	17.61	4.85	1.25	1.25

Table 3 : Evolution of the percentage of droplets lost per numerical image due to droplet aggregation phenomenon after the creation of the numerical image

$\Delta(px)$ $[mm]$ / $\overline{n_{2D}}$ $[cm^{-2}]$	**0.1**	**0.05**	**0.025**	**0.0167**
100	3.91	1.02	0.27	0.10
500	18.51	4.90	1.24	0.45
1 000	34.43	9.65	2.47	0.92
2 000	59.41	18.55	4.92	1.85
3 000	76.93	26.82	7.27	2.74
4 000	88.62	34.39	9.61	3.64

Table 4 : Evolution of the percentage of droplets lost per numerical image due to droplet merging phenomenon after the Mie scattering image processing

Declaration of interests

☐The authors declare that they have no known competing financial interests or personal relationships that could have appeared to influence the work reported in this paper.

☒The authors declare the following financial interests/personal relationships which may be considered as potential competing interests:

Lola Rousseau reports financial support was provided by Région Occitanie.